**POLITECNICO**

MILANO 1863

# Growth of iron phthalocyanine molecules on $Cr_2O_3$/Cu(110)

## Tesi di Laurea Magistrale in
## Engineering Physics - Ingegneria Fisica

Author: **Matteo Panzeri**

Student ID: 944588
Advisor: Prof. Andrea Picone
Co-advisors: Prof. Alberto Brambilla
Academic Year: 2021-22

# Abstract

The field of Spintronics, also known as spin-electronics, promises to go beyond conventional electronics by taking advantage not only of the charge, but also of the spin of the electrons. Conventional spintronic approaches are based on inorganic semiconductors; however, in these recent years, a new approach that considers organic semiconductors (OSCs) has been developed. Organic semiconductors present a higher spin relaxation time of carriers with respect to their inorganic counterparts, which makes OSCs well-suited for the transport of spin-polarization into ferromagnetic (FM) and antiferromagnetic (AF) electrodes. Moreover, a peculiar property of Organic Spintronics is the spin-dependent hybridization that occurs at the interface between the organic and the magnetic layer, which allows to tune the spin polarization and the magnetism at the interface, to govern the spintronic response of the device. This system, which behaves like a spin-polarized electrode, has been dubbed *spinterface*.

The aim of this thesis work is to study the properties of an organic layer of iron phthalocyanines on antiferromagnetic $Cr_2O_3$. The growth of chromium oxide has also been studied on two different substrates, Cu(110) and Cu(111). The chemical properties of these systems have been investigated through Auger Electron Spectroscopy and X-Ray Absorption Spectroscopy (XAS), while structural, morphological, and magnetic properties have been studied through Low Energy Electron Diffraction (LEED), Scanning Tunneling Microscopy (STM) and X-Ray Magnetic Circular Dichroism (XMCD).

The results show that the quality of $Cr_2O_3$ is higher on Cu(110) rather than on Cu(111), with islands that tend to grow larger as the coverage increases. The XAS measurements of $Cr_2O_3/Cu(110)$ confirm that the oxide grows with the right stoichiometry. An FePc thin film has been grown on $Cr_2O_3/Cu(110)$, but it has been possible to observe an ordered layer only for sub-monolayer coverage. However, XMCD measurements have shown that the interaction between the molecular film and the oxide induces a spin-polarization in the $Fe^{2+}$ $2p$ states and stabilize a ferromagnetic ordering of the $Fe^{2+}$ ions belonging to the molecular overlayer.

**Keywords:** Organic Spintronics, Spinterface, Scanning Tunneling Microscopy, XMCD

# Abstract in lingua italiana

La Spintronica è una disciplina che ha per obiettivo il superamento dell'elettronica convenzionale sfruttando non solo la carica, ma anche lo spin dell'elettrone. L'approccio della Spintronica convenzionale si basa su semiconduttori inorganici; tuttavia, negli ultimi anni è stato sviluppato un approccio diverso, basato su semiconduttori organici. I semiconduttori organici presentano tempi di rilassamento dello spin più elevato rispetto ai corrispettivi inorganici, il che li rende dei buoni candidati per il trasporto di correnti di spin polarizzate in ferromagneti (FM) e antiferromagneti (AFM). Un'altra proprietà caratteristica dei semiconduttori organici è l'ibridizzazione spin-dipendente degli stati elettronici che si verifica all'interfaccia tra il film organico e quello magnetico. Grazie a ciò è possibile controllare la polarizzazione dello spin e il magnetismo dell'interfaccia, in modo da poter controllare le proprietà spintroniche del dispositivo. Questo sistema, che si comporta come un elettrodo polarizzato in spin, è stato chiamato *spinterface*.

Lo scopo di questa tesi è quello di studiare la crescita di un film organico di ferro ftalocianine su $Cr_2O_3$. Anche la crescita dell'ossido di cromo è stata caratterizzata su due diversi substrati, Cu(110) e Cu(111). Le proprietà chimiche sono state caratterizzate attraverso spettroscopia Auger (AES) e XAS (X-Ray Absorption Spectroscopy), mentre le proprietà morfologiche e magnetiche sono state caratterizzate tramite Low Energy Electron Diffraction (LEED), Microscopia ad Effetto Tunnel (STM) e X-Ray Magnetic Circular Dichroism (XMCD).

I risultati ottenuti mostrano che l'ossido di cromo cresce in modo migliore su Cu(110) invece che su Cu(111), formando isole che tendono ad allargarsi via via che viene aumentato il coverage. Le misure di XAS su $Cr_2O_3$/Cu(110) mostrano che l'ossido cresce sul substrato con la corretta stechiometria. È stato cresciuto un film sottile di FePc su $Cr_2O_3$/Cu(110), tuttavia è stato possibile ottenere un film ordinato solo per coverage inferiori al monolayer. Le misure XMCD hanno mostrato però che l'interazione tra l'ossido e il film organico induce una polarizzazione dello spin negli stati $2p$ degli ioni $Fe^{2+}$ e permette di ottenere un ordinamento ferromagnetico di questi ioni del film organico.

**Parole chiave:** Spintronica Organica, Spinterface, Microscopia STM, XMCD

# Contents

# 1 | Introduction

The aim of this introductory chapter is to present the theoretical and experimental background that motivated this thesis. The first section gives a rapid overview of Organic Spintronics by presenting the properties of the interface between the molecular films and ferromagnetic layers (also known as *spinterfaces*).

The second section presents the peculiarities of antiferromagnetic Spintronics and of the spinterfaces between molecules and antiferromagnetic layers, which are the objects of this experimental work. Finally, in the last two sections an overview of iron phthalocyanine (FePc) molecules and chromium oxide ($Cr_2O_3$) will be given.

## 1.1. Organic Spintronics

The field of Spintronics, also known as spin-electronics, promises to go beyond conventional electronics by taking advantage not only of the charge but also of the spin of electrons. It is a vast field that contains different topics, and the ideal spintronics experiment mainly consists of three main actions (see Figure 1.1): a non-equilibrium spin population is generated within the material (injection); then, an external stimulus is used to control the spins in the desired way (manipulation). Finally, the results of the manipulation should be detected (detection). Each of these steps can be carried out in several ways, using electrical and/or optical methods depending on the materials. Applying the electron spin instead of (or in combination with) the electron charge allows for the design of non-volatile devices, in which logic operations, storage, and communication can be combined. Spintronic devices are also potentially faster and less power-consuming than conventional electronic devices, since the relevant energy scale for spin dynamics is considerably smaller than that for manipulating charges [2].

Spin-related phenomena have been studied on transition metals and inorganic semiconductors [1], but in recent years the attention has been driven to other classes of materials, among which organic materials have shown very interesting properties. Organic semiconductors (OSCs) have been tested as spintronic devices only in the last decade because of their promising potential applications in electronic devices, including organic light-
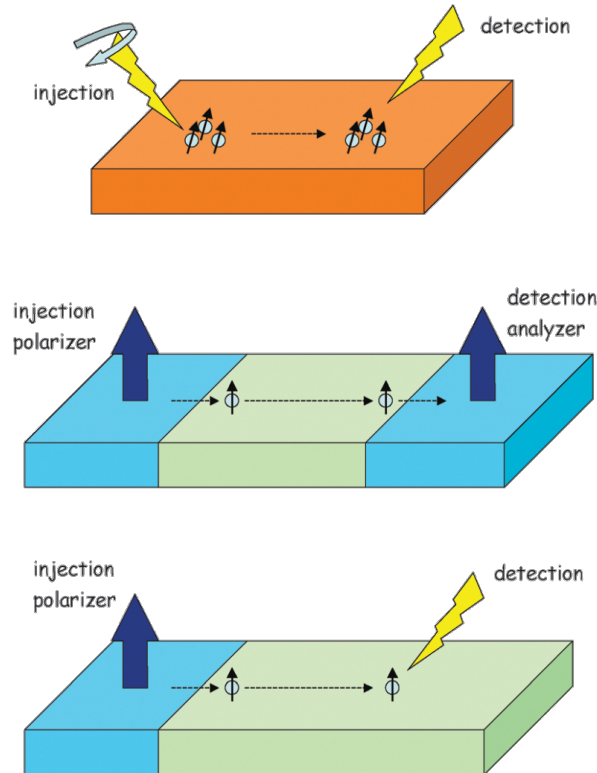
Figure 1.1: Different methods for studying spins in spintronics experiments. The creation of spin-polarized wave packets can be performed optically in inorganic semiconductors. Detection can be performed by magnetic metals. Also, there can be hybrid strategies, for example electrical injection and optical detection. Reprinted from [1].

emitting diodes (OLEDs) [3] and organic field-effect transistors [4]. The main advantage of OSCs for spintronic applications is the long spin relaxation time of carriers that results from the small spin-orbit coupling. Organic semiconductors are usually small molecules or $\pi$-conjugated polymers and they usually possess weak spin-orbit coupling since they are mostly composed of light materials such as carbon, oxygen, and hydrogen (see Figure 1.2). Spin relaxation times up to a millisecond have been achieved [5]. This is a very promising aspect of potential applications of OSCs in Spintronics because it allows for electrical control of the spin dynamics and, due to the very long spin relaxation time, multiple operations on the spins can be performed before they reach equilibrium [2]. Another advantage resides in the possibility of building flexible, low-cost devices [6], with the perspective of scaling the devices down to the molecular scale.

Moreover, organic materials offer a significant advantage with respect to their inorganic counterparts because the almost unlimited degrees of freedom in molecular design offer the possibility to synthesize molecules with specific electronic, optical, and magnetic
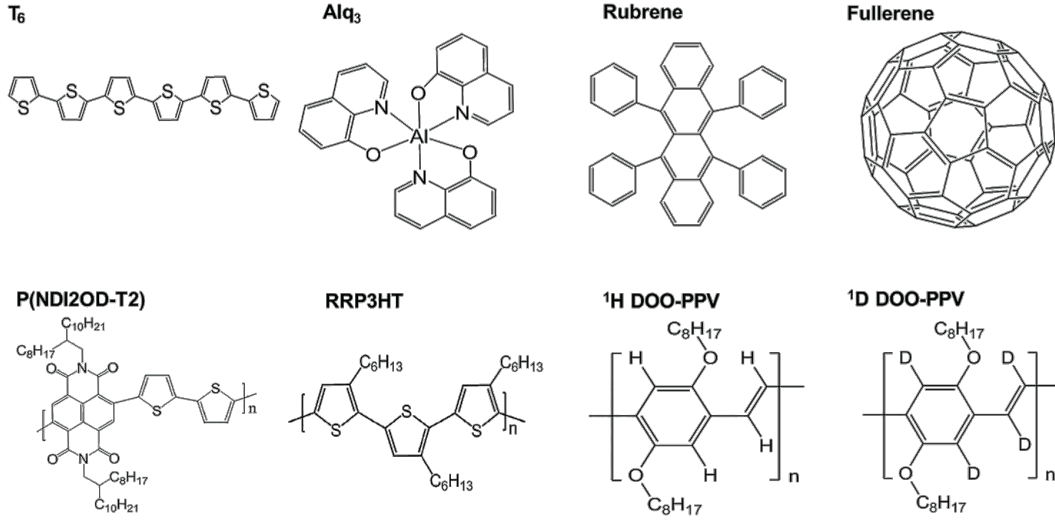
Figure 1.2: Examples of organic semiconductors. Reprinted from [7].

properties [8]. Molecules are therefore quasi-0D building blocks that form 2D layers onto inorganic materials held together by weak forces such as Van der Waals or dipole-dipole forces. Also, self-assembled, crystalline, organic films can be built at the interface.

### 1.1.1. Spinterfaces

The spin-dependent hybridization that occurs at the interface between the organic and the magnetic layer allows to tune the spin polarization and magnetism of the interface, thus governing the spintronic response of the device [9]. When organic molecules are brought in proximity of a ferromagnetic (FM) metallic layer, the molecular levels become hybridized by coupling with the electronic states of the metal. Since the electrons in the molecular levels have a certain probability of escaping into the metal, the energy molecular levels are now finite with a lifetime $\tau$. As a consequence, the levels broaden with finite width $\Gamma = \hbar/\tau$ and shift to an effective energy value (Figure 1.3). The results of the interaction on the molecular levels are dependent on the DOS of the FM metal. Since the FM metal DOS is spin-polarized, the molecular DOS at the interface is also expected to be spin-polarized. Such a system behaves as a spin-polarized electrode and it has been named *Spinterface* [10]. Thus, it is possible to define the spin polarization at the interface $P_{int}$ as a function of the spin-polarized interfacial DOS $D_{int}^{\uparrow(\downarrow)}$:

$$P_{int} = \frac{D_{int}^{\uparrow} - D_{int}^{\downarrow}}{D_{int}^{\uparrow} + D_{int}^{\downarrow}} \tag{1.1}$$
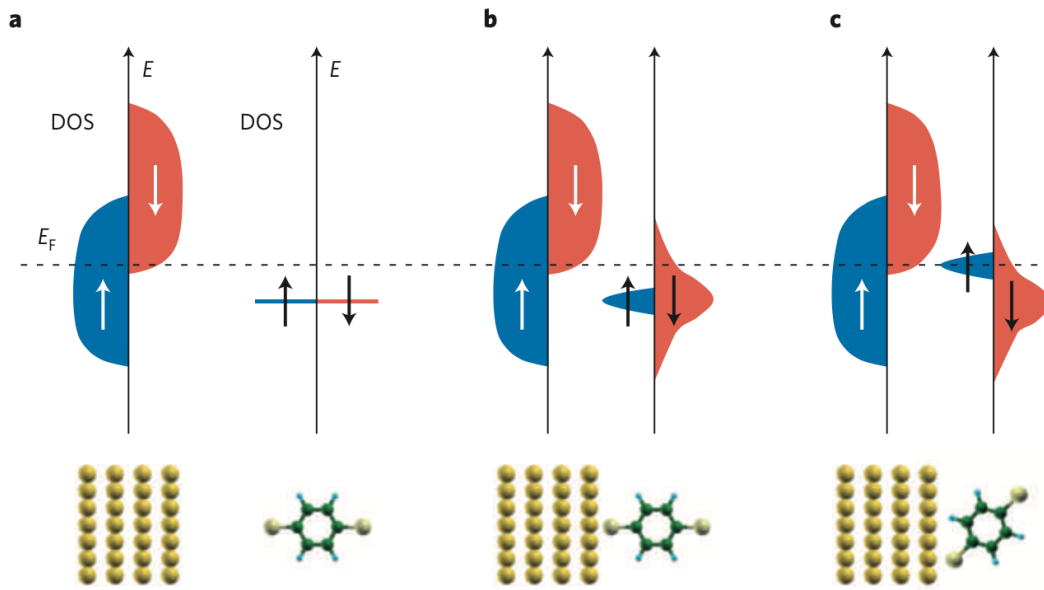
Figure 1.3: Schematic of spin hybridization at an organic/inorganic interface. (a) The metal and the molecules are well separated, the molecular DOS is a series of discrete states while the metal DOS is spin-polarized. (b) The molecule is brought close to the metallic surface and the energy levels broaden. (c) Also, due to the interaction with the metal, the molecular energy levels shift. Reprinted from [10].

This spin-polarization at the interface can be drastically different from that of the FM electrode. This happens because the lifetime, and therefore the broadening, of the molecular level depends on the degree of interaction between the molecule and the electrode. Since the spin-up and spin-down bands of the FM layer are shifted from each other in energy, the spin-up and spin-down molecular levels are broadened by different amounts: this can result in a situation where the broadened molecular level around $E_F$ has opposite spin-polarization than that of the majority electrons in the FM (Figure 1.3(b)).

Another way to tune the spin-polarization at the interface comes from the shifting of the molecular energy levels. The strength and the type of interaction between the molecular and the FM layers cause the spin-dependent shift of molecular levels, so that a particular spin-polarized molecular level can end up at $E_F$, as it happens for instance in Figure 1.3(c) for the majority component of the spin-polarized Highest Occupied Molecular Orbital (HOMO).

It is expected that such insights can lead to the molecular-level engineering of metal/organic interfaces to customize spin injection for bringing new electrical functionalities to the spintronic devices. In the past years, many studies have investigated the properties of ferromagnetic/organic spinterfaces. High spin polarization has been observed in several systems, for example Co(001)/amorphous C [11], Ni(111)/$C_{60}$ [12]. Fullerenes have also

proven successful in overcoming the Stoner criterion by inducing room temperature magnetization of Cu and Mn films [13].

Phthalocyanine (Pc) molecules are among the most promising class of molecules for building and engineering spinterfaces: a spin-polarization $P \approx 80\%$ has been observed in Co/MnPc spinterface (Figure 1.4) at room temperature, and the explanation for this result is that the dominant interfacial hybridization mechanism involves states at (or near) $E_F$ from the ferromagnet and the molecule that are present only in one spin channel [14]. Spinterfaces constitute a strong candidate for exploring and exploiting phenomena that
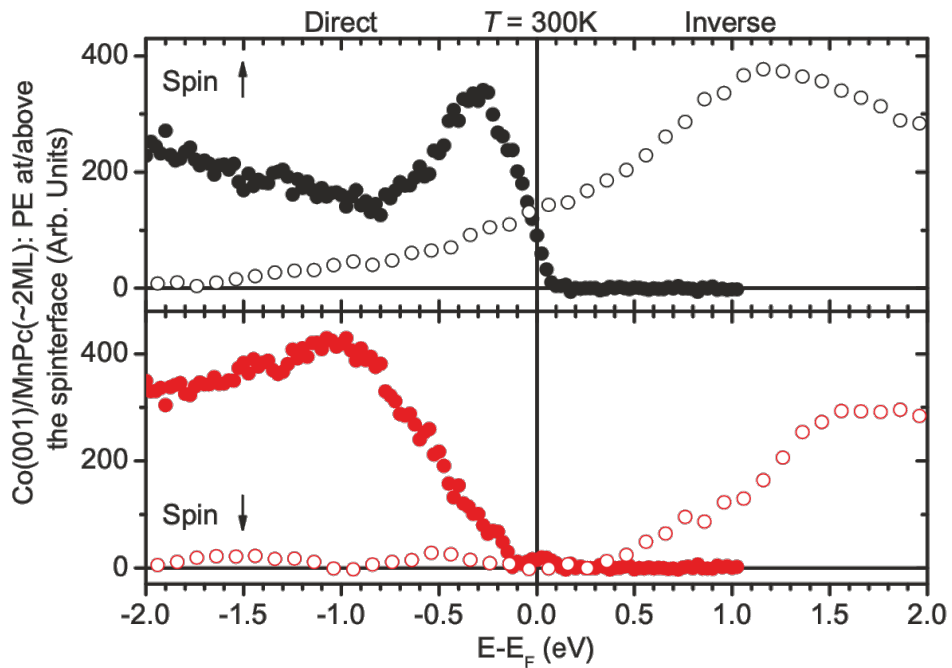


Figure 1.4: (Spin-resolved difference spectra of direct (closed symbols; hn 5 20 eV) and inverse (open symbols) photoemission (PE) spectroscopy at room temperature of Co/MnPc (2 ML for direc PE, 2.6 for inverse PE) reveal a $P \approx 80\%$ at $E_F$. Reprinted from [14].

are otherwise unreachable with current spintronic systems because of the possibility of developing a new class of devices in which molecular hybrid interfaces play an active role, translating various externally controllable input signals into new physical and chemical functionalities. The change in hybridization strength by external stimuli such as light or electric voltages will lead to a net change of properties of the inorganic layer, modifying the device's relevant parameters. Controlling these parameters in a reversible way opens up new perspectives for new device exploration [15].

## 1.2.    Antiferromagnetic Spintronics

This section wants to present the advantages of Spintronics using antiferromagnetic (AF) materials instead of ferromagnets. The first part introduces this topic and explains why antiferromagnets can be more useful than ferromagnets in certain spintronic applications. The second part briefly introduces some results regarding organic-antiferromagnetic spinterfaces, in analogy to what was already presented in Section 1.1.1.

### 1.2.1.    Advantages of antiferromagnfetic Spintronics

Conventional spintronic devices are based on the control of magnetic moments in ferromagnets. Antiferromagnetic Spintronics, as the name suggests, deals with antiferromagnets. The recent discovery of the electrical switching (Figure 1.5) of an antiferromagnet suggests, for example, that antiferromagnetic moments can be controlled in microelectronic devices by means comparably efficient to ferromagnets [16].

Antiferromagnets are magnetically ordered, but the neighbouring magnetic moments point in opposite directions, thus resulting in zero net magnetization. This is already a great advantage with respect to ferromagnets, since this means that antiferromagnets do not produce stray fields and they are insensitive to external magnetic field perturbations. A potential application could come, for instance, in the field of memory for computing: magnetic memory elements made of antiferromagnetic materials can be more closely packed, leading to higher storage density. Moreover, the peculiar spin dynamics of AFs allow for faster devices with respect to their FM counterparts [18].

In addition, the number of materials that show in nature AF ordering is much higher than those that show FM ordering. Many transition metal oxides are antiferromagnetic, including NiO, CoO and $Cr_2O_3$. Among metallic antiferromagnets, Mn-based alloys, such as FeMn, PtMn and IrMn are the most important ones.

A key difference is found in the dynamics of antiferromagnets and ferromagnets. The former materials are characterized by more complex and faster dynamics than in FMs [19]. Antiferromagnets have two magnetic sublattices with opposite magnetizations. Even though it is possible to depict an antiferromagnet as two interpenetrating ferromagnets, the inter-sublattice exchange makes the dynamics of AFs richer than that of FMs. As depicted in Figure 1.6(a), a uniform static field in an AF generates torques that have an opposite sign and that compensate for each other.

An efficient way of generating oscillations of the staggered magnetization $\mathbf{L} = \mathbf{M_1} - \mathbf{M_2}$ in AFs is the spin-transfer torque (STT) [17]. When the polarization of the spin current is perpendicular to the staggered magnetization, it generates parallel torques on the op-
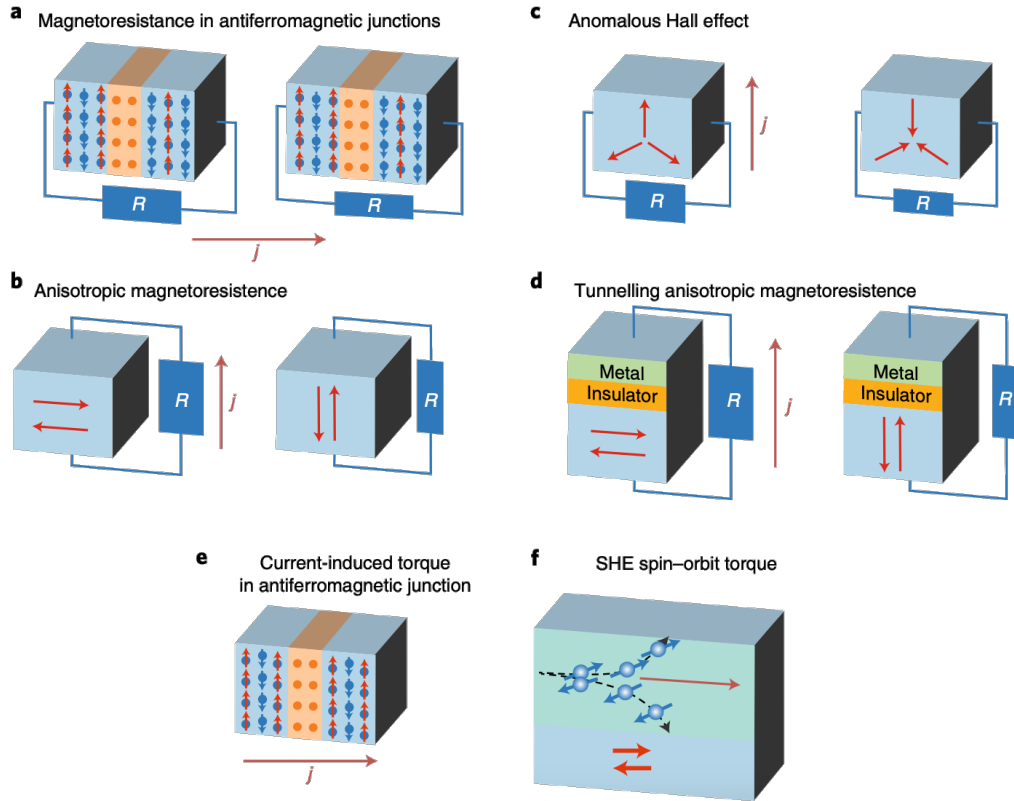
Figure 1.5: Schematic of various concepts proposed for electrical manipulation of anti-ferromagnetic order. (a) Magnetoresistance in AF spin valves or tunneling junctions; (b) Anisotropic magnetoresistance (AMR); (c) Anomalous Hall effect; (d) Tunneling anisotropic magnetoresistance (TAMR); (e) Spin-transfer torque in AF spin valves or tunneling junctions; (f) Spin-Hall effect (SHE) spin-orbit torque. Adapted from [17].

posite magnetic sublattices (Figure 1.6(a)). These torques can induce a stable precession of **L** within the plane perpendicular to the spin-current polarization. Thus, while the FM driven by a magnetic field or a spin-polarized current tends to switch between different static states, an AF is a natural spin-torque oscillator. The typical frequency of such an oscillator falls into the THz range, making AFs attractive for applications [19]. The collective spin precessions are also known as spin waves (or magnons). Spin waves carry spin currents but they do not contribute to heat flow [20]. There are several differences between ferromagnetic and antiferromagnetic spin waves. Spin waves always carry a spin in FMs, thus a magnon flux is equivalent to a spin current. In AFs, however, spin waves may not carry a spin. Spin waves can be linearly or circularly polarized, in linearly polarized spin waves the average spin is zero. Circularly polarized waves, however, carry a spin with opposite orientation for clockwise and anticlockwise polarizations.

Another aspect that makes antiferromagnetic spin waves very attractive for potential
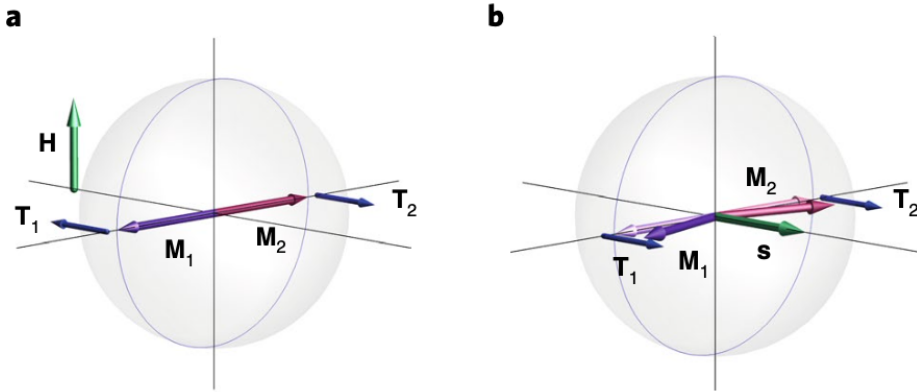
Figure 1.6: In antiferromagnets, the sublattice magnetizations $\mathbf{M}_1$ and $\mathbf{M}_2$ are antiparallel in equilibrium. (a) A magnetic field $H$ generates the antiparallel torques $\mathbf{T}_{1,2}$, which compensate each other and block magnetization dynamics. (b) The current with spin polarization $\mathbf{s}$ generate the parallel torques $\mathbf{T}_{1,2}$ that tilt sublattice magnetizations $\mathbf{M}_{1,2}$ forward and cause rotation of magnetic sublattices. Adapted from [19].

technological applications is that they can be excited not only by purely electric signals, but also by magnetic THz pulses [21] and by ultrafast optical pump systems [22], again reinforcing the relevance of antiferromagnets for data storage and processing.

### 1.2.2.   Antiferromagnetic spinterfaces

Antiferromagnetic substrates have been used to replace ferromagnetic ones in the design of spintronic devices due to their hard magnetic property, the lack of magnetic stray fields, and their relative insensitivity to external magnetic fields. As it was pointed out in Section 1.1.1, organic materials are very promising for spintronic devices because the interaction between the organic and the ferromagnetic layers can alter the spin-polarization properties of the interface and act, for instance, as a spin filter. This spin-polarized interface is called spinterface.

For this reason, the studies of organic spinterfaces have also turned their attention to the characterization of the organic/antiferromagnetic interface. The results that have been obtained thus far confirm that the organic/antiferromagnetic interface behaves in a similar manner to the ferromagnetic counterpart. As an example, it was shown that when $H_2Pc$ (phthalocyanine) molecule adsorbed on antiferromagnetic Mn(001) substrate, due to spin-dependent hybridization, a strong, negative, giant magnetoresistance (GMR) is observed [23].

The behaviour of MnPc molecules adsorbed on antiferromagnetic IrMn(001) was studied in another work, and it was shown that a small hybridization can be obtained, but an

interesting result is the reversible switch of the negative/positive spin polarization predicted through compression/elongation of the Mn–N bonds of the MnPc molecule [24]. Finally, $C_{60}$ (fullerenes) molecules have also shown promising results in this topic: it was shown that when fullerenes are adsorbed on antiferromagnetic Cr(001) they can trigger the reconstruction of the Cr surface, while the $p$-$d$ orbitals interaction between $C_{60}$ and Cr induces spin-splitting of the Lowest Molecular Orbital (LUMO) states around $E_F$. The spin-polarization that arises in the reconstructed surface is compared to the unreconstructed case [25], as shown in Figure 1.7.
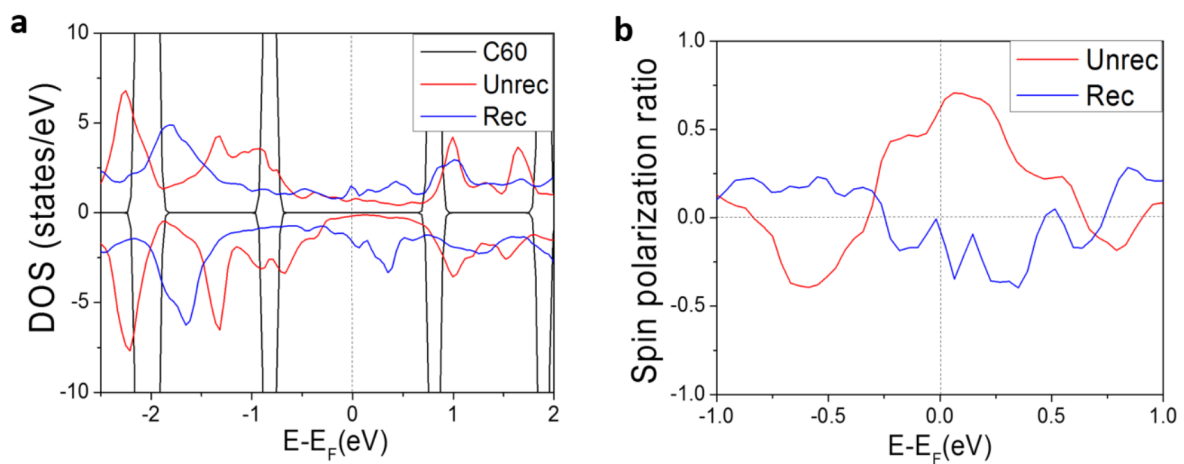


Figure 1.7: (a) Spin-polarized density of states (DOS) of $C_{60}$ in the unreconstructed and reconstructed structures on Cr(001) and of gas phase $C_{60}$. (b) Spin-polarization ratio (SPR) of $C_{60}$ in the unreconstructed and reconstructed cases on Cr(001). Reprinted from [25].

## 1.3.   Iron phthalocyanine (FePc) molecules

This section gives an overview of iron phthalocyanine (FePc) molecules that will be one of
the objects of study in the experimental part of Chapter 3. In this section, the chemical
and structural properties of metallophthalocyanines will be presented, as well as their
electrical, optical and magnetic properties.

### 1.3.1.   Structure

Phthalocyanines (Pc) have been studied for many years especially for the preparations of
dyes, paints and pigments. However, in the last years phthalocyanines have caught the
attention of researchers for potential technological applications due to their electronic,
magnetic and optical properties.

The structure of planar phthalocyanines consists of four isoindole groups linked together
by an inner porphyrazine ring. The simplest, metal-free, phthalocyanine molecule ($H_2Pc$)
has two H atoms in the centre of the porphyrazine ring, as depicted in Figure 1.8(a). These
hydrogen atoms are referred to as pyrrolic H atoms. In the simple metallophthalocyanine
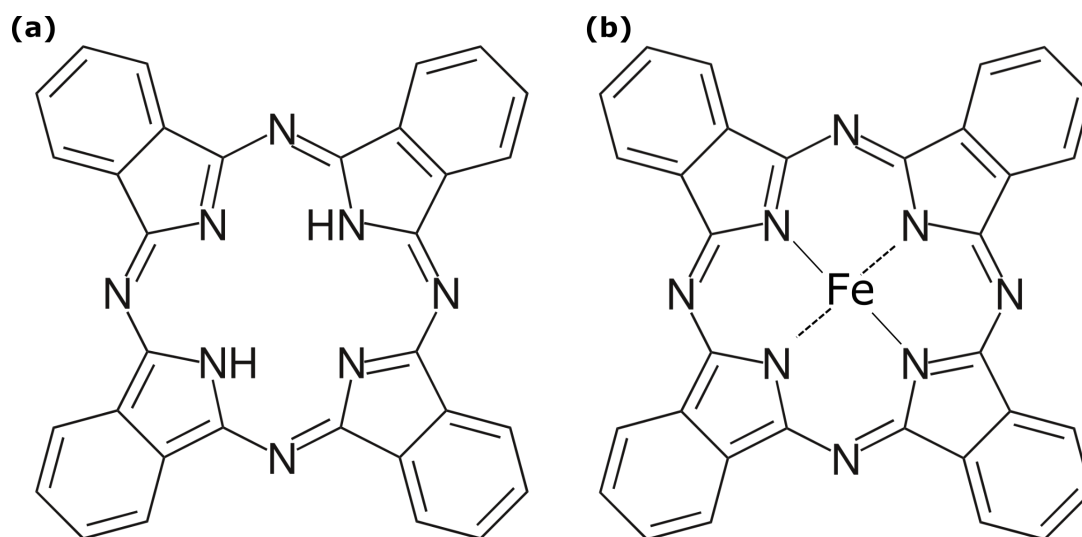(MPc), the two H atoms are replaced by a single metal atom. An important property



Figure 1.8: Structure of simple phthalocyanine, $H_2Pc$; (b) Structure of iron phthalocya-
nine, FePc. Adapted from: `https://en.wikipedia.org/wiki/Phthalocyanine`

related to this structure is that, generally, the various metallophthalocyanine molecules
are thermally stable and thus can be sublimed without decomposition. This means that,
in contrast to many other organic compounds, the preparation of phthalocyanine thin
films by vacuum evaporation is feasible [26].

This high thermal and environmental stability, together with the possibility of incorporating around 70 different metal atoms into the phthalocyanine rings to optimize the physical response, made this class of molecules a very promising candidate for device applications. Metallophthalocyanines have been studied as targets for gas sensors, optical devices, light-emitting devices, and optical information recording media [27].

### 1.3.2. Magnetic Properties

Iron phthalocyanine (FePc), represented in Figure 1.8(b) is a member of MPcs family that presents $Fe^{2+}$ as a central atom. It is a dark blue material. FePcs have caught the attention of researchers for their magnetic properties: an early study in 1967 showed that the $Fe^{2+}$ ion has a ground state that corresponds to the $S = 1$ triplet state and that the value of $\mu_{eff}$ is 3.71 $\mu_B$ [28]. Further studies have found that $Fe^{2+}$ ions are strongly magnetically coupled in FePc into ferromagnetic chains, with the weak interchain coupling leading to a soft molecular ferromagnet, a behaviour that is similar to another metallophthalocyanine, MnPc. FePcs are thus valid candidates for potential Organic Spintronics applications as they represent examples of molecular magnets [29].

### 1.3.3. Electrical Properties

The electrical properties of phthalocyanines have been studied extensively to show the behaviour of these molecules as low-dimensional semiconductors. The conductivity of metallophthalocyanines can be due to either the intrinsic properties of a particular molecule or to the organization of molecules with an extended orbital overlap. For instance, the stacking of metallophthalocyanines enables electron delocalization through the $\pi$-$\pi$ orbital overlapping. In the solid state, some phthalocyanines behave as molecular organic semiconductors with slight $p$ or $n$ character [30]. In the case of an iron phthalocyanine thin film, studies of the thermoelectric power have shown that it behaves as $p$-type semiconductor in which the mobility of the positive free charges is greater than that of the negative carriers. The electron-hole mobility ratio $\mu_e/\mu_h$ was found to be around 0.25 in the temperature range 300-450 K [31].

### 1.3.4. Optical Properties

A very useful approach in optical sensing is the one based on the charge absorption/emission properties of a chemical reagent when in contact with an analyte. Such reagent must have a very high absorption coefficient and exhibit fluorescence emission with sufficiently high quantum yield. Phthalocyanines have proven to be very effective materials for optical

detection. The macrocycle has intense visible region absorption (called the Q-band) and, depending on the central atom, good fluorescence emission. More than 90% of photoreceptors in laser copiers/printers are phthalocyanines [32]. In the case of FePcs, the Q-band absorption is near 620 nm, with three other peaks at 560, 630, and 720 nm. There is also another absorption band near 350 nm called B-band [33], as depicted in Figure 1.9.
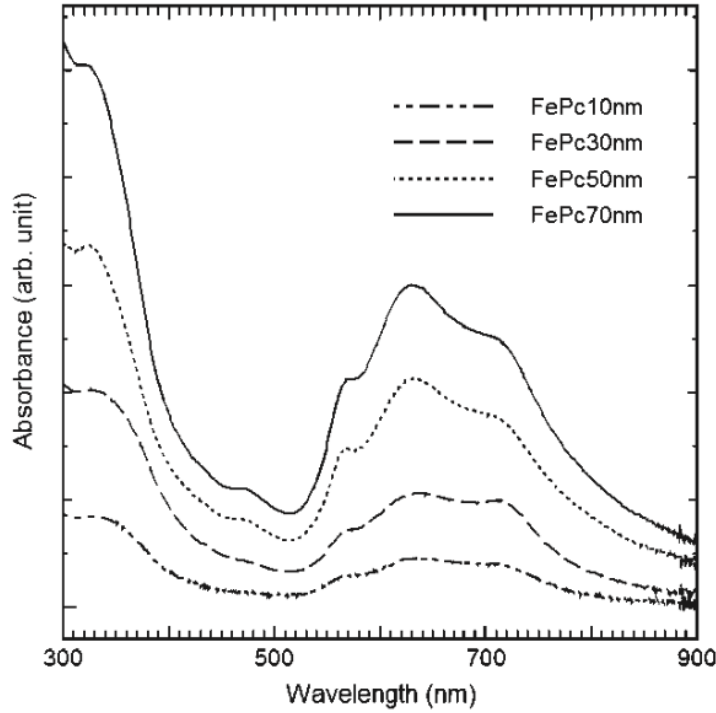


Figure 1.9: Optical absorption spectra of FePc for various film thicknesses. Reprinted from [33].

FePcs have been employed in third-harmonic generation experiments since they exhibit a third-order susceptibility $\chi^{(3)}$ [34]. Phthalocyanines exhibit excellent nonlinear optical response for both second and third-order effects [32]. The majority of the studies have focused on third-order nonlinear optics with Pcs, since they are centrosymmetric compounds. The difficulties with the second-order harmonic generation with phthalocyanine reside in the difficulty of preparing non-centrosymmetric molecules.

## 1.4. Chromium Oxide

Chromium oxide ($Cr_2O_3$) is another object of study in this thesis work. This section covers the structural, electronic, and magnetic properties of $Cr_2O_3$.

### 1.4.1. Structural and magnetic properties

Chromium oxide has several important applications: it is a catalyst, and it has been used in chemical gas sensors, coating masks, solar energy absorbers, and magnetic recording media [35]. Chromium oxide crystallizes in a corundum (rhombohedral) structure, as shown in Figure 1.10. This crystal structure can be described as a hexagonal closed-packed array of oxygens in which the Cr atoms occupy 2/3 of the interstitial octahedral sites [36]. Cr atoms also form a hexagonal lattice, but the Cr and O lattices are rotated by 90°.
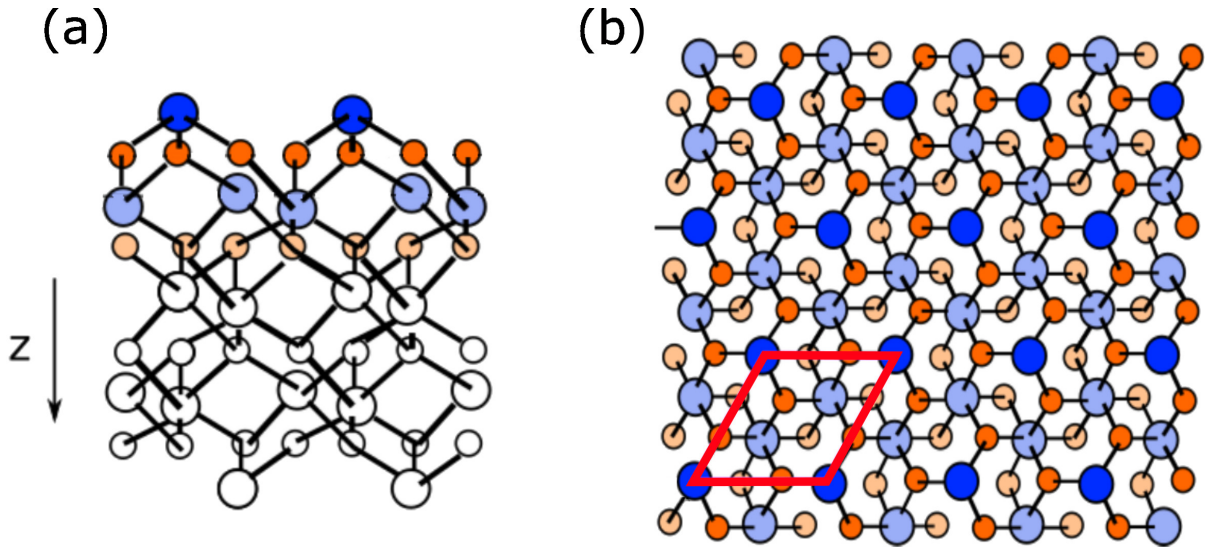


Figure 1.10: Side (a) and top (b) views of $Cr_2O_3$ structure. The hexagonal arrangement of Cr (blue) and O (orange) atoms can be observed. The lattice parameter of the cell, highlighted in red, is 4.96 Å.

As it is visible from Figure 1.10(b), the lattice parameter of O atoms is different than that of Cr atoms. The proportionality factor between O and Cr lattice parameters can be derived from purely geometrical consideration, and it is found to be $1/\sqrt{3}$.
The lattice parameters of the rhombohedral structure are $a = b = 4.96$ Å, and $c = 13.81$ Å, where $a$ and $b$ are the sides of the rhombus (highlighted in red in Figure 1.10(b)), while $c$ is the height of the unit cell which corresponds to 6 layers of $Cr_2O_3$ along the (0001) direction. The oxygen lattice parameter is $a_O = 2.86$ Å.

Chromium oxide is antiferromagnetic with a Neel Temperature $T_N = 307$ K. The corresponding magnetic structure, represented in Figure 1.11, is the $+ - + -$ spin sequence on the $Cr^{3+}$ atoms along the rhombohedral axis $c$. This type of antiferromagnetic ordering corresponds to the minimum energy configuration, whilst other possible AF configurations, such as $+ + - -$, or $+ - - +$ ($Fe_2O_3$ type), are less stable [36]. The computed magnetic moment of Cr is $m_{Cr} = 2.66$ $\mu_B$, in accordance with experimental values of 2.76 $\mu_B$ and 2.48 $\mu_B$. Oxygen atoms have no net magnetic moment [37].
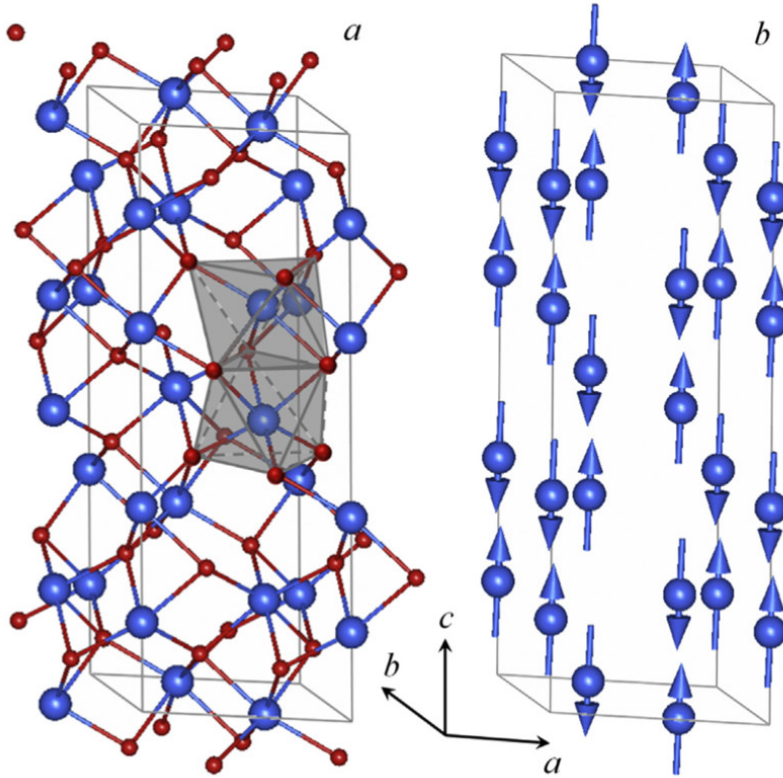


Figure 1.11: Side view (a) and magnetic structure (b) of $Cr_2O_3$. Reprinted from [38].

### 1.4.2. Electronic Properties

Chromium oxide is an insulator with experimental band gap $E_g = 3.2$ eV. It is an ionic solid with $Cr^{3+}$ and $O^{2-}$ ions. The atomic effective charges calculated are, however, $q_{Cr} = 1.73|e|$ and $q_O = -1.15|e|$: This deviation from the ionicity ($+3|e|$ and $-2|e|$) are interpreted as due to covalent contribution of the bonding [37].

Along the trigonal [0001] axis, three layers of oxygen are alternated with two chromium layers in the stacking sequence Cr-Cr-$O_3$-Cr-Cr- $\cdots$. The (0001) surface can be obtained by cleaving the crystal in any of these layers, therefore three chemically different termina-

tions are possible. These three terminations are called metal-rich, bulk, and oxygen-rich terminations and they are represented in Figure 1.12. The most stable termination is the bulk termination (Figure 1.12(b)), in which the surface is terminated by a single layer of Cr, while the other two terminations are not stable due to the excess of defect or charge density, and are only stable at high temperature and oxygen partial pressure [37].
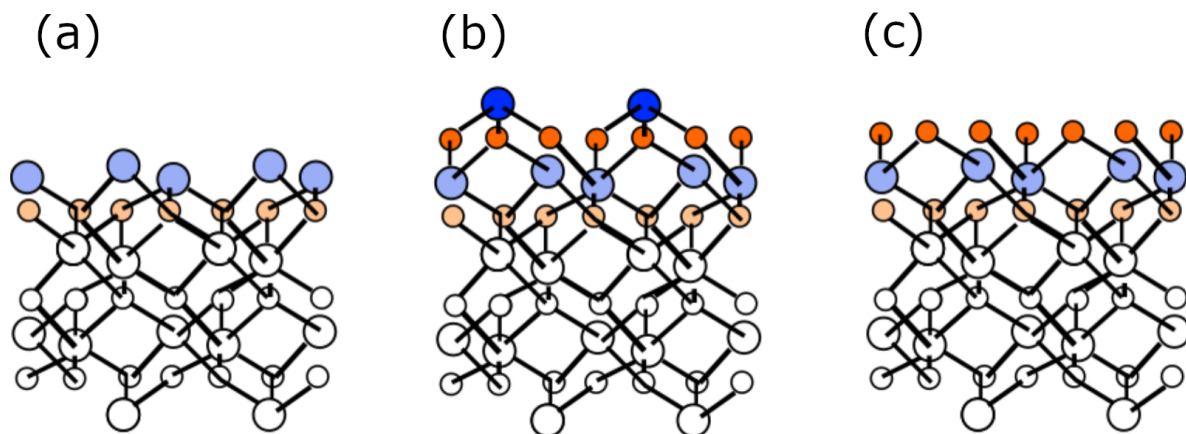


Figure 1.12: Possible terminations of $Cr_2O_3$: (a) metal-rich; (b) bulk; (c) oxygen-rich.

# 2 | Experimental Methods

The majority of the measurements presented in this work were performed at the STM Laboratory, located in the Physics Department of Politecnico di Milano. The experimental setup consists of two Ultra High Vacuum (UHV) chambers: one is dedicated to the *in situ* sample preparation and characterization via Low Energy Electron Diffraction (LEED) and Auger Electron Spectroscopy (AES), and the other one is dedicated to Scanning Tunneling Microscopy (STM) and Spectroscopy (STS).

X-Ray Absorption Spectroscopy (XAS) and X-Ray Magnetic Circular Dichroism (XMCD) measurements, on the other hand, were performed at APE-HE beamline located in Elettra synchrotron facility in Trieste. This beamline can also perform *in situ* preparation of the samples.

## 2.1.  Ultra High Vacuum Technology

All of the experimental techniques employed in this thesis require Ultra High Vacuum conditions. UHV regime is an essential condition for surface physics [39]. When performing experiments, it is necessary to have surfaces with a negligible amount of contaminants for a sufficiently long time. This is unfeasible in normal pressure conditions because the surface would be contaminated or oxidized in very short time. The time required for the contamination of a surface under UHV conditions (that is, with pressures below $10^{-9}$ mbar) is greater than $10^3$ s. A typical UHV setup consists of steel chambers pumped by a combination of several different pumps, since each of them can operate only in a limited pressure range. It is also of primary importance that the experimental setup is constantly pumped, otherwise it would not be possible to maintain UHV regime.

The UHV chamber available at the STM laboratory employs four types of pumps: rotary, turbo-molecular, ionic, and titanium-sublimation pumps.

### 2.1.1.   Rotary pump

The rotary pump is used to establish an initial vacuum condition, by bringing down the pressure from atmospheric to around $10^{-2}$ mbar. Rotary pumps are based on a rotor that changes the volume of the gas by eccentric rotation and it forces the gas out of the chamber, as schematized in Figure 2.1.
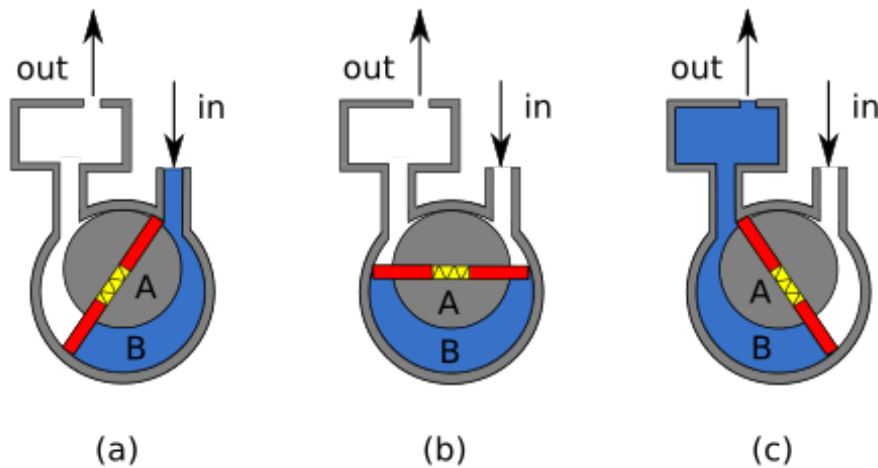


Figure 2.1: Schematic of the working principle of a rotary pump. The gas is expanded during the inlet phase (a) until, after rotation, it is separated from the chamber (b). During the outlet phase (c), the gas is compressed and forced out of the chamber. Reprinted from: `https://it.wikipedia.org/wiki/Pompa_per_vuoto_rotativa`

### 2.1.2.   Turbo-molecular pump

Turbo-molecular pumps extract gas molecules from the UHV chamber by means of a high-speed rotor (15000 to 30000 rpm) to the exit, where they are pumped away by the rotary pump. The rotor blades are inclined with respect to the rotation axis (see Figure 2.2) to maximize the number of molecules moving from the chamber to the exit and not in the opposite direction.

### 2.1.3.   Ion pump

Rotary and turbo-molecular pumps are employed when a large amount of gas has to be pumped out. Their pumping efficiency decreases for light molecules such as $H_2$. Moreover, they generate vibrational noise that can interfere with delicate measurements like STM. Ion pumps (Figure 2.3) are used to solve this problem. They consist of steel tubes arranged
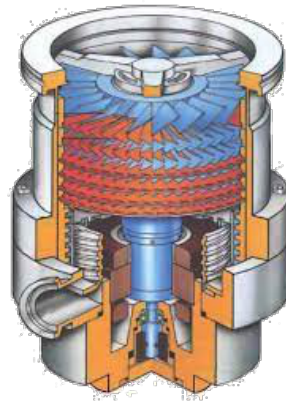
Figure 2.2: Illustration of a turbo-molecular pump.
Reprinted from `https://www.buschvacuum.com/documents/10180/403438/Busch_Instruction_Manual_Turbo_TM_1100_A_en_0870564260.pdf`

in a multicell structure acting as anodes. These cells are sandwiched between a cathode made of Ti plates. Finally, a permanent magnet generates a magnetic field between the anode and the cathode. Electrons are emitted from the cathode and they are accelerated to the anode due to a high voltage (between 3 and 7 kV) applied to the anode. The trajectory of electrons is helicoidal due to the presence of the magnetic field, maximizing the possibility of collision with gas molecules. When this happens, the molecules are ionized and accelerated to the cathode, where they are trapped or chemisorbed.
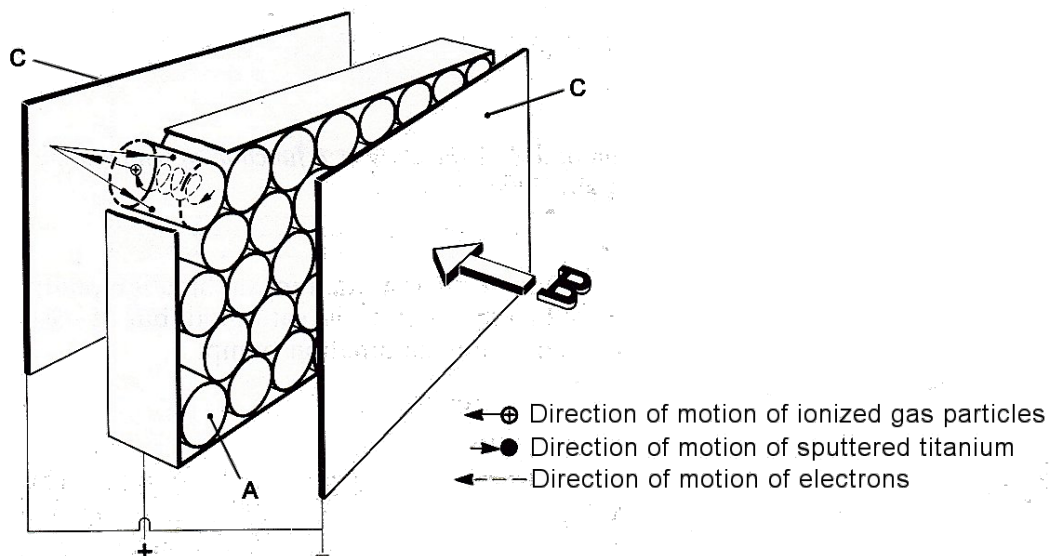


Figure 2.3: Schematic of an ion pump. Reprinted from: `https://www.book-vacuum-science-and-technology.com/vacuum-pumps-and-pumping-systems/`

### 2.1.4.    Titanium sublimation pump

Titanium sublimation pumps are composted by Ti-Mo alloy filaments in which a very high current ($I \simeq 50$ A) flows. This causes the sublimation of the filament which then condensates on the chamber walls, confining the remaining gas molecules. This is the most effective way of pumping very light gas molecules such as $H_2$.
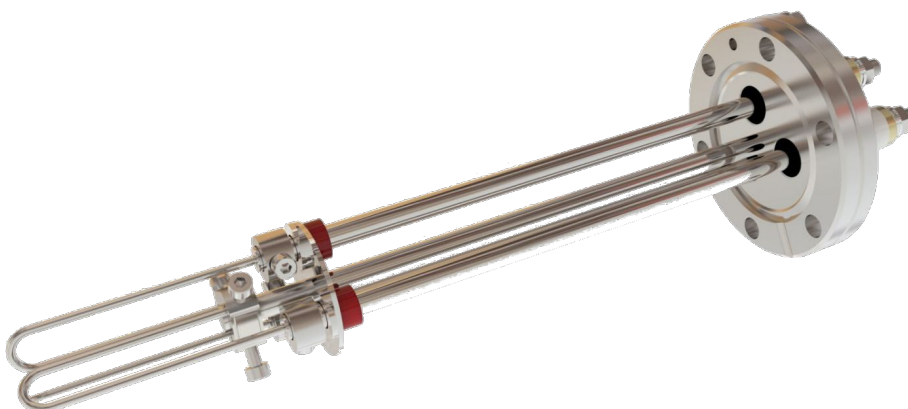


Figure 2.4: Image of a titanium sublimation pump. Reprinted from `https://vacgen.com/head-sublimation-pump-3-filament-dn38cf`

## 2.2.    Low Energy Electron Diffraction (LEED)

LEED is an experimental technique that is used to retrieve qualitative, and possibly quantitative, information regarding the structure of a surface in solids. With this technique, it is also possible to obtain information about the arrangement of atoms or molecules which are adsorbed on the surface.

### 2.2.1.    Physical Principles

During a LEED experiment, a mono-energetic electron beam is sent to the surface of the sample, and the back-scattered electrons are collected by a fluorescent screen. If the surface is well ordered, it will act as a diffraction grid and it will be possible to observe diffraction spots on the screen. This principle is explained in the so-called kinematic theory of diffraction, in which the electrons that are elastically scattered by the surface only once are considered.

In the framework of kinematic theory the electron beam is considered as a plane wave

with De-Broglie wavelenght:

$$\lambda_0 = \frac{h}{\sqrt{2mE}} \tag{2.1}$$

where $h$ is the Planck's constant, $m$ is the electron mass and $E$ is the energy. The wave vector associated to the electron is then $k_0 = 2\pi/\lambda_0$, in order to have diffraction the Laue condition must be satisfied:

$$|\vec{k}| = |\vec{k_0}| \ , \ \vec{k} = \vec{k_0} + \vec{K} \tag{2.2}$$

here $\vec{k}$ is the wave vector of the elastically back-scattered electron and $\vec{K}$ is the reciprocal lattice vector [39]. In order to visualize how the diffraction pattern would appear on the fluorescent screen, one can construct a sphere with radius $\vec{k_0}$ in the reciprocal space known as the Ewald sphere. The set of $\vec{k_0}$ satisfying 2.2 will be made by those vectors that start from the centre of the sphere to the interception between the sphere surface and any reciprocal lattice $\vec{K}$ vector, as represented in Figure 2.5. Thus, the LEED image will reproduce
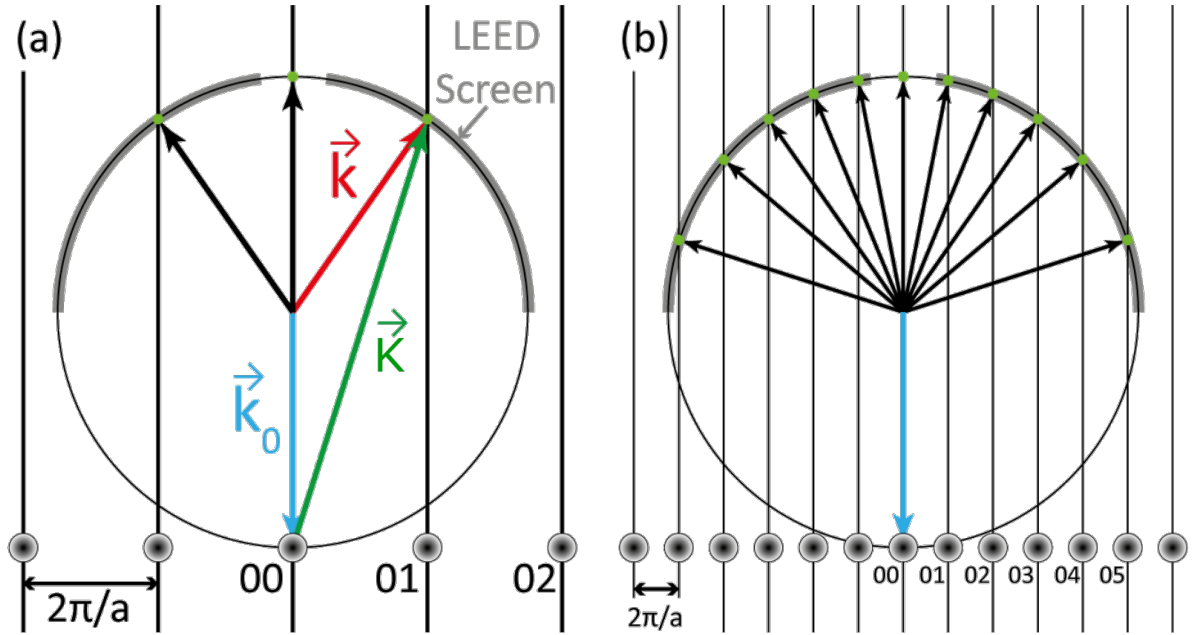


Figure 2.5: Representation of the Ewald sphere for lower (a) and higher (b) energies. Adapted from `https://www.maths.tcd.ie/~bmurphy/thesis/thesisse2.html`

the lattice in the reciprocal space, that is the Fourier transform of the real lattice. The relationship between the real and the reciprocal lattice is represented in Figure 2.6 in the case of a simple square lattice with and without a superstructure. In this schematic, it is important to underline that in the case of a superstructure with a periodicity that is twice the periodicity of the substrate, its correspondent in the reciprocal space (i.e. the LEED pattern) will have half of the periodicity with respect to the substrate.
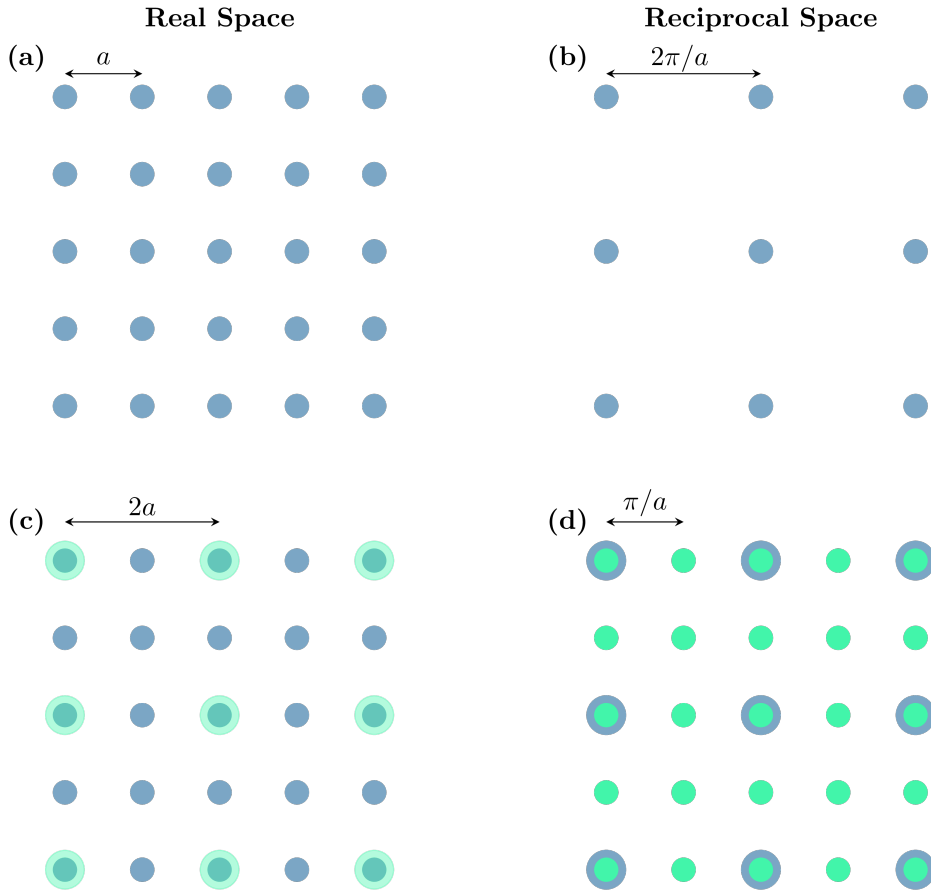
Figure 2.6: Schematic of a simple square lattice in the real space (a),(c) and its LEED correspondence in the reciprocal space (b),(d) with and without a $(2 \times 2)$ superstructure.

### 2.2.2.  Experimental Setup

In the STM laboratory, the experimental setup for LEED coincides with the AES setup. As schematized in Figure 2.7, it is composed of an electron gun that emits electrons via thermionic effect from a $LaB_6$ filament, a multi-grid system, and a set of focusing lenses. The multi-grid system has the purpose of selecting only the elastically scattered electrons; to do so, the first and the last grids are grounded while the middle one is kept at a negative potential. The fluorescent screen is kept at a high voltage (around 5 kV) to accelerate the electrons and stimulate fluorescent emission. The typical energies employed for LEED measurements range from 25 to 200 eV. Images are acquired with a CCD camera.
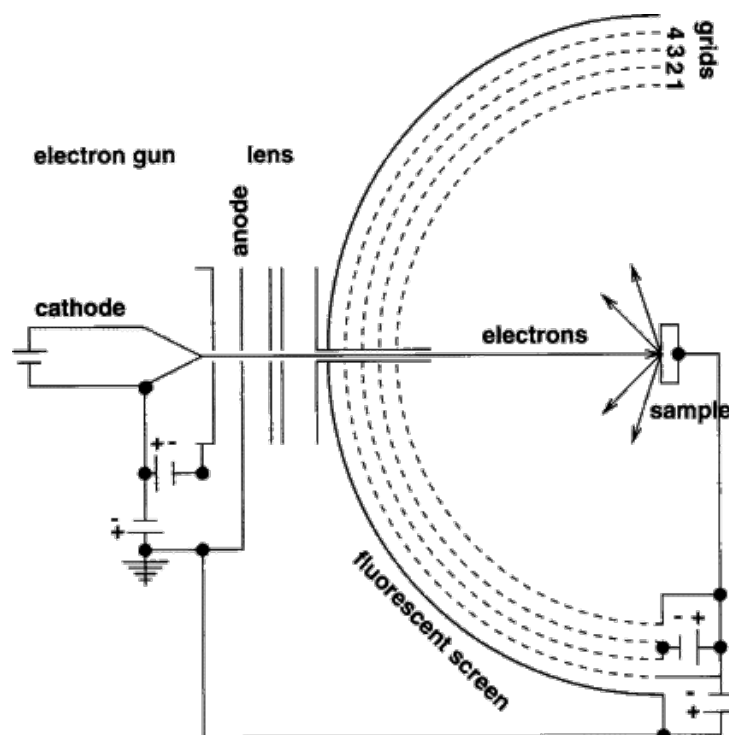
Figure 2.7: Scheme of a LEED experimental setup. Reprinted from: `https://www.sciencedirect.com/topics/chemistry/low-energy-electron-diffraction`

## 2.3. Auger Electron Spectroscopy (AES)

Auger Electron Spectroscopy (AES) is a technique that is useful for analyzing the chemical composition and stoichiometry of the first layers of the sample.

### 2.3.1. Physical Principles

The physical principle underlying AES is the Auger Effect. If a hole is created in the valence shell, it can be filled by an electron in the outer shell; when this happens, a photon of energy $h\nu = E_{out} - E_{core}$ may be emitted. Here, $E_{out}$ is the energy of the outer shell electron (i.e. the valence electron), and $E_{core}$ is the energy of the core-shell electron. This excess of energy may also be directly transferred to another electron (which is called Auger electron), that is emitted with kinetic energy:

$$E_{kinetic} = E_{core} - E_{binding} - \Phi \tag{2.3}$$

where $E_{binding}$ is the binding energy of the electron and $\Phi$ is the work function of the material. The hole in the core level required for stimulating Auger electron emission

is created by sending a high energy electron beam onto the sample, as schematized in Figure 2.8. Since the energy levels are discrete and they are different in each element, one can identify a specific chemical element from the set of energies of the Auger electrons emitted from a sample. The characteristic Auger peaks of elements and compounds are listed in reference books.
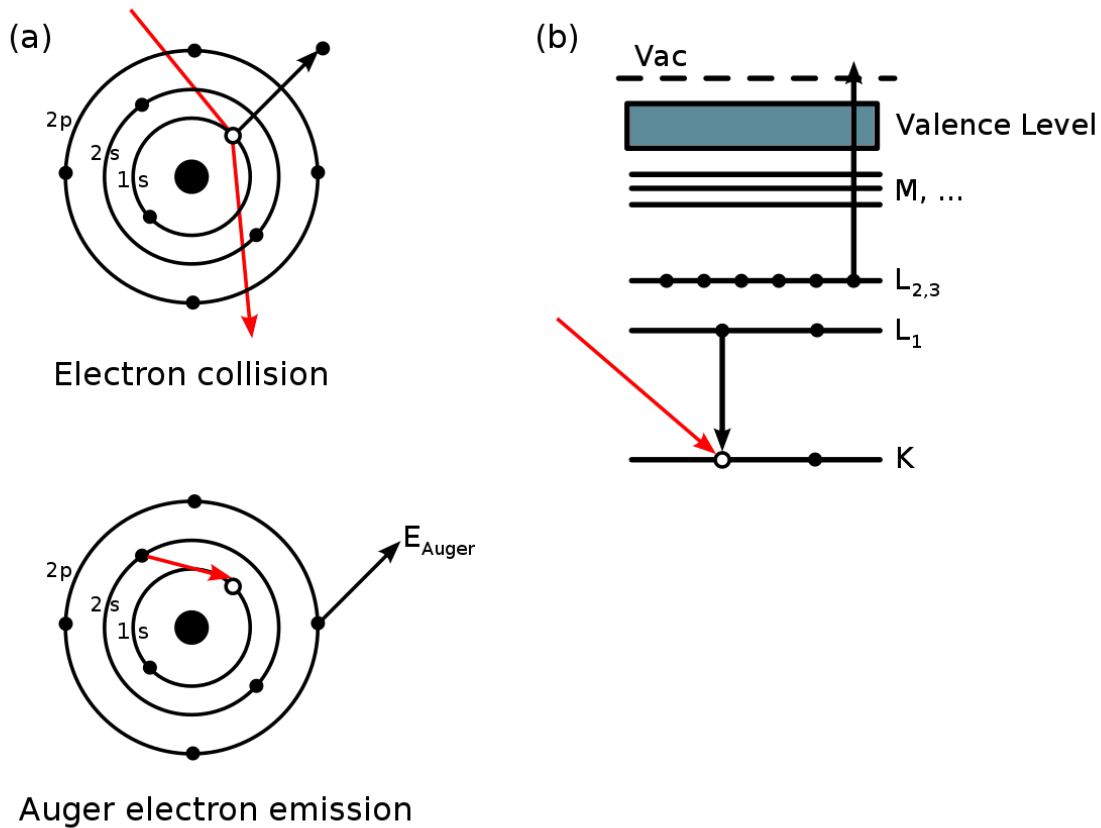


Figure 2.8: Scheme of an Auger process (a) and energy scheme of a $KL_1L_{2,3}$ Auger transition (b). Adapted from: `https://en.wikipedia.org/wiki/Auger_effect`

### 2.3.2.  Experimental Setup

The experimental setup for AES is the same as the one used for LEED experiments, and it consists of an electron gun, a set of focusing lenses, and an electron detector.

Electrons are emitted by thermionic effect from a $LaB_6$ filament. A Wehnelt electrode is kept at a negative potential with respect to the filament to favour the extraction of electrons. Then, the emitted electrons are accelerated and focused on the sample surface thanks to a set of focusing lenses, which are kept at a positive potential. As explained

in Section 2.3.1, this electron beam is responsible for the formation of core holes within the sample. The Auger electrons are then collected by a detector, obtaining the signal $N(E)$, which is the number of electrons at a certain energy $E$. This is not the only signal collected by the detector, as one has to also take into account secondary and scattered electrons which cause background noise that limit AES sensitivity. The solution to this problem is to perform the derivative $dN/dE$ of the signal, thus obtaining clear Auger peaks while minimizing the noise.

In reality, the detector acquires the signal:

$$I(E) \propto \int_{E}^{E_b} N(\varepsilon)\, d\varepsilon \tag{2.4}$$

where $E_b$ is the energy of the electron beam and $E = e \cdot V$, where $V$ is the potential applied to the grids. The signal acquired is a current signal, therefore a double differentiation is required to retrieve the quantity corresponding to $dN/dE$.
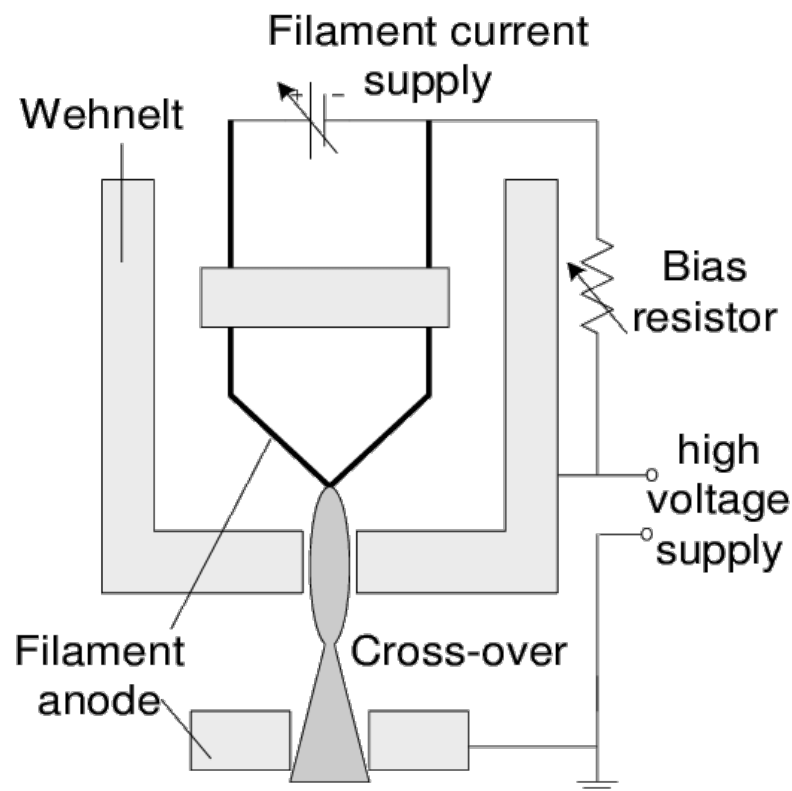


Figure 2.9: Scheme of a thermionic source of electrons. Reprinted from: `https://www.researchgate.net/figure/Thermionic-Electron-gun_fig1_263298392`

## 2.4.  Scanning Tunneling Microscopy (STM)

Scanning Tunneling Microscopy (STM) is a powerful scanning probe technique developed in the Eighties by Binning, Rohrer, Gerber, and Weibel. It allows to study the surface morphology of a conductive sample down to the atomic scale by exploiting the tunneling of electrons from a tip to the sample (and *vice versa*) in presence of a voltage difference between the tip and the sample.

The variation of this very small current, called tunneling current, is exploited to obtain the topography of the surface.

### 2.4.1.  Physical Principles

The physical principle of STM is a purely quantum-mechanical effect known as the tunnel effect. Differently from classical physics, a quantum particle has a non-zero probability of passing through a potential barrier. This tunneling probability decreases very rapidly, so that it is completely negligible for a macroscopic system, but it becomes relevant at the nanoscale.

In an STM experiment, the tunneling effect is exploited by keeping the sample surface and the microscope tip at a very close distance; then, a potential difference is applied to cause the flow of electrons from the sample to the tip through vacuum or *vice versa*, depending on the sign of the voltage, as represented in Figure 2.10. The sign of the bias voltage, therefore, is a useful parameter to probe the empty states of the tip or of the sample.

The shape of the microscope tip is of great importance: if the tip is very sharp it will end with a single atom and the tunneling current will flow mainly from the apex atom of the tip to the sample, so that the contributions from farther atoms can be neglected. In this condition, the current flowing through the barrier is:

$$I_t = \frac{4\pi e}{\hbar} \int_{-\infty}^{\infty} \rho_s(E)\rho_t(E - eV)T(d, E, V)[f(E) - f(E - eV)] \, dE \tag{2.5}$$

where $V$ is the applied voltage, $\rho_s(E)$ and $\rho_t(E - eV)$ are the densities of states of sample and tip, $\hbar$ is the reduced Planck's constant, $f(E)$ is the Fermi-Dirac distribution and $T(d, E, V)$ is the tunneling probability for electrons, given by:

$$T(d, E, V) = \exp\left[-\frac{2d}{\hbar}\sqrt{2m(\Phi - E + \frac{1}{2}eV)}\right] \tag{2.6}$$

As highlighted by Equation 2.6, the tunneling probability has an exponential dependence on the sample-tip distance $d$. Also, from Equation 2.5 it should be noted that the tunneling current depends on the density of states of the sample, which should be different from zero around the Fermi level, meaning that it is not possible to perform STM measurements on insulating samples.
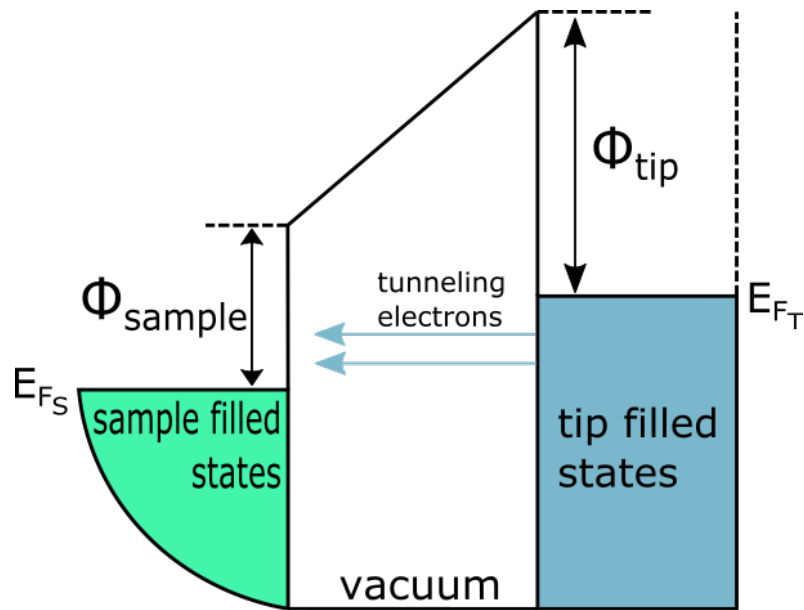


Figure 2.10: Tunneling of electrons from tip to sample.

## 2.4.2.   Experimental Setup

The experimental setup of an STM system is represented in Figure 2.11. The tip movement is controlled by a piezoelectric tube with a sub-Å precision. The movement of the piezoelectric can be either in the $x$ - $y$ plane or in the $z$ direction.

An STM measurement can be performed in two ways, which are constant current mode and constant height mode. The former is the most used and, as the name suggests, it consists in maintaining a constant tunneling current during the scan by adjusting the sample-tip distance. With this technique it is possible to map the surface morphology of the sample. The latter consists in keeping a constant sample-tip distance and in registering the current variation. The tunneling current signal is detected by the electronic components and it is then processed via software (*Matrix* in this case) to obtain the image. Finally, a damping system is required to limit the vibrations coming from the external environment.
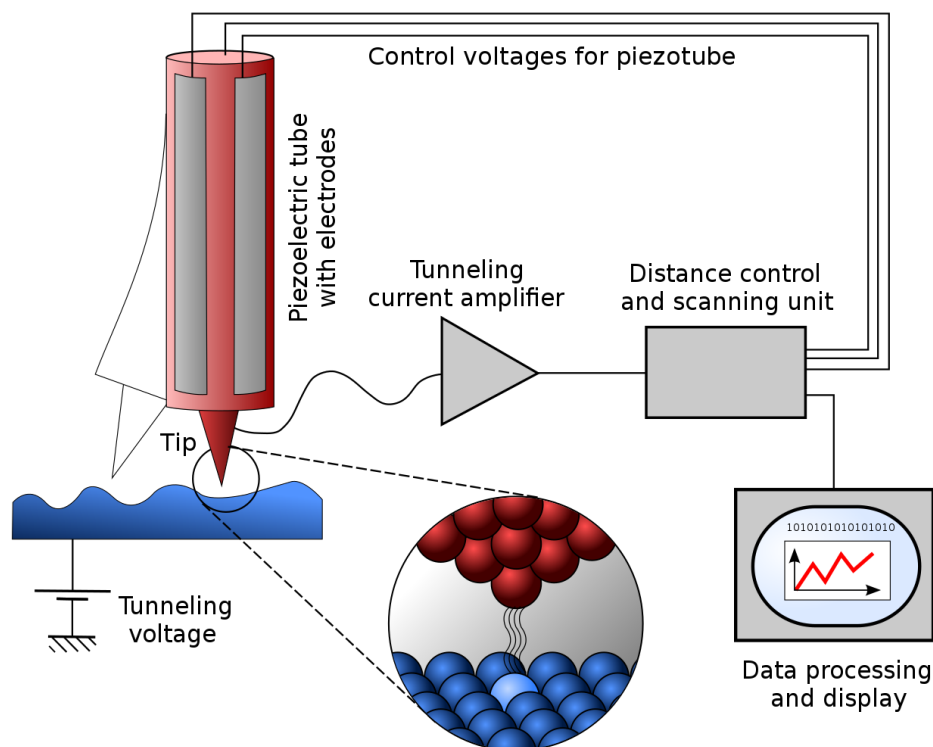
Figure 2.11: Schematic representation of STM setup. Reprinted from: `https://en.wikipedia.org/wiki/Scanning_tunneling_microscope`

## 2.5.   X-Ray Absorption Spectroscopy (XAS)

XAS is an experimental technique that provides the measurement of the X-Ray absorption behaviour of a material as a function of the energy. In order to perform a XAS measurement, a high-intensity, coherent X-Ray beam is required. The beam must also be tuneable over a certain energy range; for this reason, XAS measurements are carried out at synchrotron radiation facilities.

### 2.5.1.   Physical Principles

The energy of the X-Ray beam is of the order of $10^4$ eV, corresponding to wavelengths in the order of 1 Å. With this wavelength of the same order of magnitude as the interatomic distances, it is possible to have insight into the local atomic structure, in particular the local environment of each atom in a compound.

The electrons that are excited with XAS technique are core electrons typically in the 1s or 2p shells. When the X-Ray photon arrives on the atom, it can excite the core electron to a higher energy bound state, or to an unbound state; the first transition is the one

studied by XAS, while the other is studied in X-Ray Photoelectron Spectroscopy (XPS). The Lambert-Beer law is applied to introduce a very important quantity in XAS which
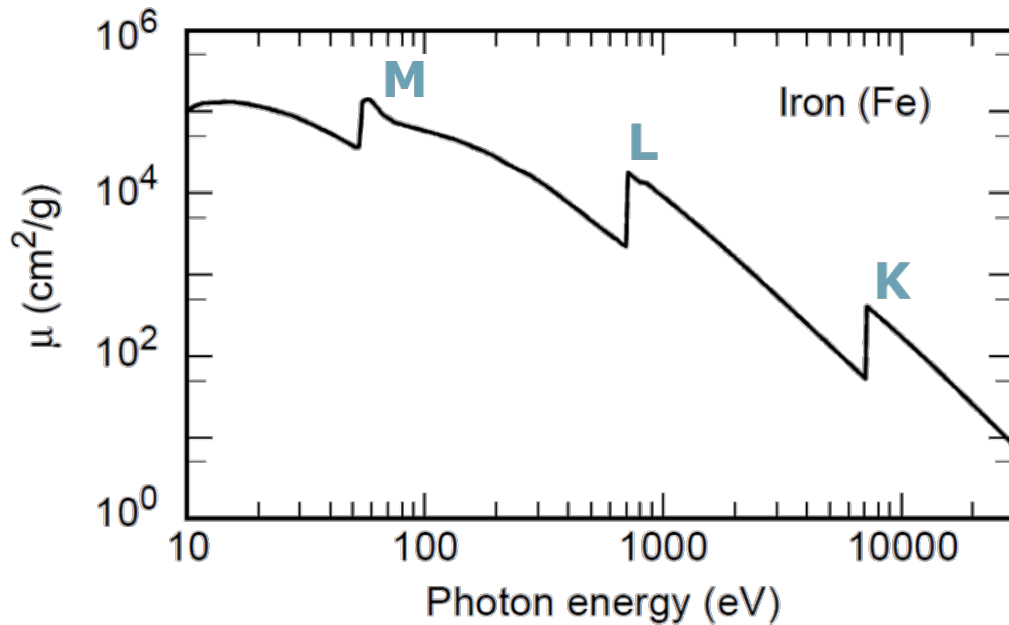


Figure 2.12: Behaviour of $\mu$ as a function of the energy in the case of Fe. Reprinted from: `https://xdb.lbl.gov`

is the X-Ray mass absorption coefficient $\mu_M$ (units $g/cm^2$):

$$I = I_0 e^{-\mu_M \rho d} \tag{2.7}$$

where $\rho$ is the mass density of the sample, $d$ is the thickness of the sample and $I$ is the intensity of the beam after passing through the absorber.

The absorption coefficient tends to decrease steadily as the photon energy increases. However, when the photon energy matches the energy for a core electron transition, $\mu$ increases sharply, as represented in Figure 2.12.

The photon energy also determines the subset of XAS that is used. As depicted in Figure 2.13, XAS is divided into two main regions:

- X-Ray Absorption Near-Edge Structure (XANES/NEXAS): it is the region near the absorption edge, where there is a sharp resonance peak. This technique is sensitive to local atomic states such as oxidation state and symmetry;

- Extended X-Ray Absorption Fine Structure (EXAFS): it is the region that appears after XANES and up to a few hundreds of eV greater than the absorption edge. The features in this region are small oscillations caused by the scattering of electrons by

neighbouring atoms. EXAFS gives information about bond lengths and chemical coordination environment.
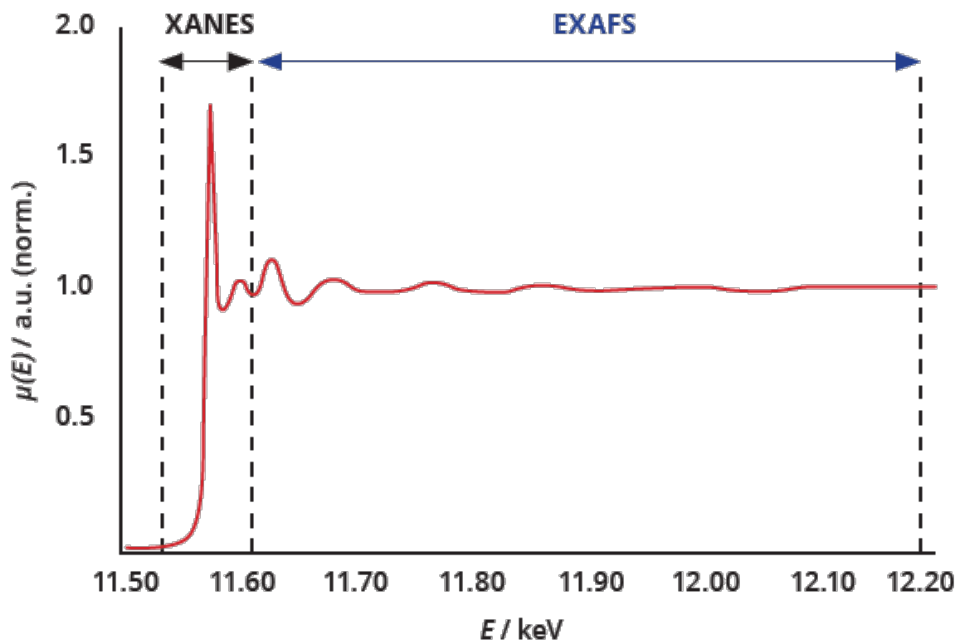


Figure 2.13: Different regions of XAS as a function of the photon energy. Reprinted from: `https://sigray.com/x-ray-absorption-spectroscopy/`

## 2.6.  X-Ray Magnetic Circular Dichroism (XMCD)

The term "dichroism" refers to changes in the absorption of polarized light that passes through a material in two different directions. Since materials typically absorb one color of white light preferentially, the material appears with two different colors for the two light directions, hence the word *di-*(two) *chroic* (colored). Nowadays, the term dichroism is used more generally to describe the dependence of photon absorption of materials on light polarization.

### 2.6.1.  Physical Principles

The origins of dichroism in materials can be due to anisotropies in charges or in the spin of the material. In this last case, we speak of magnetic dichroism. X-Ray Magnetic Circular Dichroism (XMCD) is a spectroscopic technique that probes the modification of the electronic structure of a material in the presence of magnetic order, resulting in a variation of the near-edge X-Ray absorption intensity.

Figure 2.14 illustrates the principle of XMCD. In conventional L-edge XAS, the total in-
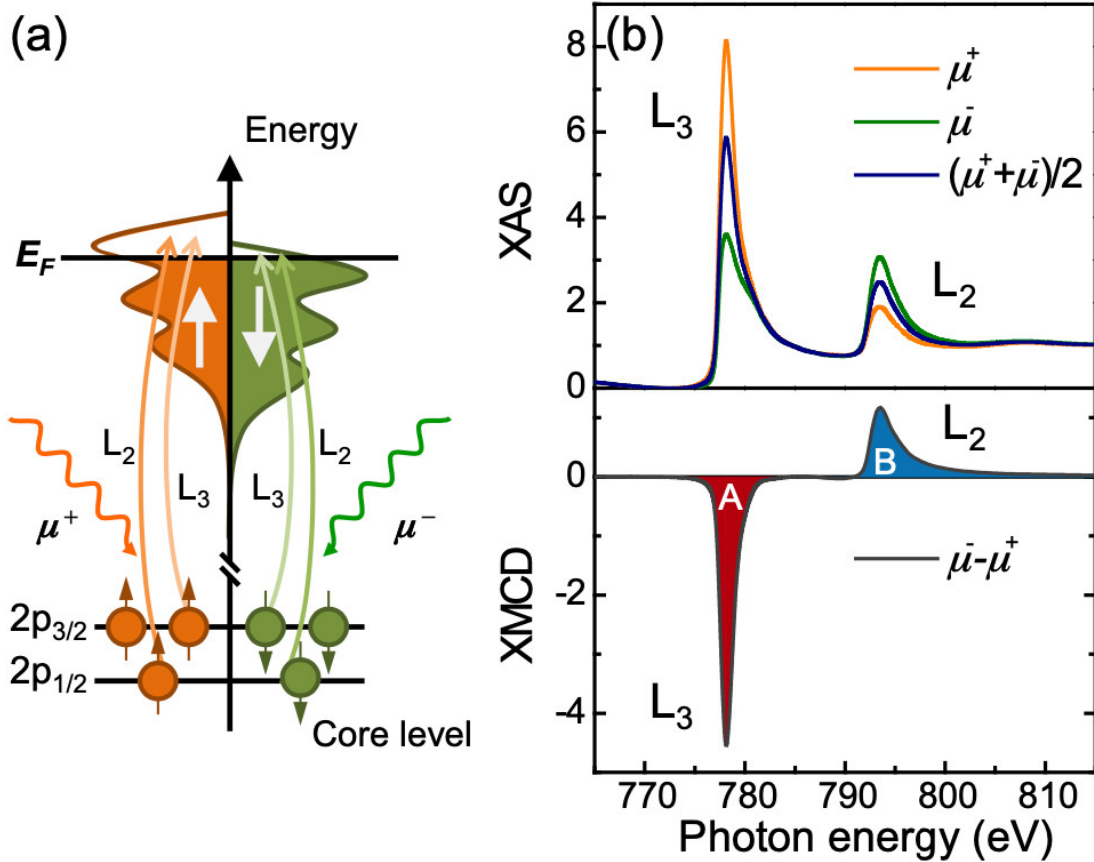
Figure 2.14: (a) Circularly polarized photons excite electrons from the spin-split $2p$ core level. Spin-polarized electrons will have to find available states in the $3d$ valence band, resulting in differences if the band is spin-polarized; (b) XAS at the $L_{2,3}$ for right $\mu^+$ and left $\mu^-$ circularly polarized light, together with the difference spectrum, the XMCD. Reprinted from [40].

tensity of $L_2$ and $L_3$ peaks is linked to the number of empty $d$ states (holes). In magnetic materials, the spin-splitting of the $d$-shell causes an imbalance of spin-up and spin-down electrons, and, equivalently, also in the available states (holes). In order to make the measure sensitive to the number of spin-up and spin-down holes, left and right circularly polarized light is used. Circularly polarized light carries angular momentum: right circular photons carry opposite angular momentum than left circular photons, hence photoelectrons with opposite spin will be created upon the absorption of these photons. Right polarized X-Rays excite 62.5% spin-up electrons from $L_3$ edge ($2p_{3/2}$), while left polarized x-rays excite 37.5% spin-up electrons. The $2p_{1/2}$ level ($L_2$ edge) gives 25% spin-up with circular right light and 75% spin-up with circular left light.

Since spin-flip transitions are forbidden in the electric dipole transition, spin-up (spin-

down) photoelectrons from the $p$ core-shell can only be excited to spin-up (spin-down) valence states (Figure 2.14(a)). Therefore, there will be different $L_2$ and $L_3$ absorption intensities for circular left and circular right light due to the spin-splitting of the valence band, as represented in Figure 2.14(b). Finally, the XMCD signal is obtained by taking the difference between the two XAS spectra.

## 2.6.2.   Experimental Setup

Both XAS and XMCD measure the absorption of X-Ray radiation as a function of the photon energy. As mentioned earlier, a high-intensity X-Ray beam which is also tuneable in energy is required to perform an XAS experiment, meaning that synchrotron radiation is required. The XAS and XMCD measurements present in this work were acquired at APE-HE beamline at Elettra synchrotron facility in Trieste. The photon energy is selected through a spherical grating monochromator. The radiation is focused in the vertical plane thanks to the spherical mirror of the monochromator and in the horizontal plane thanks to a toroidal mirror, and it is then sent onto the sample.
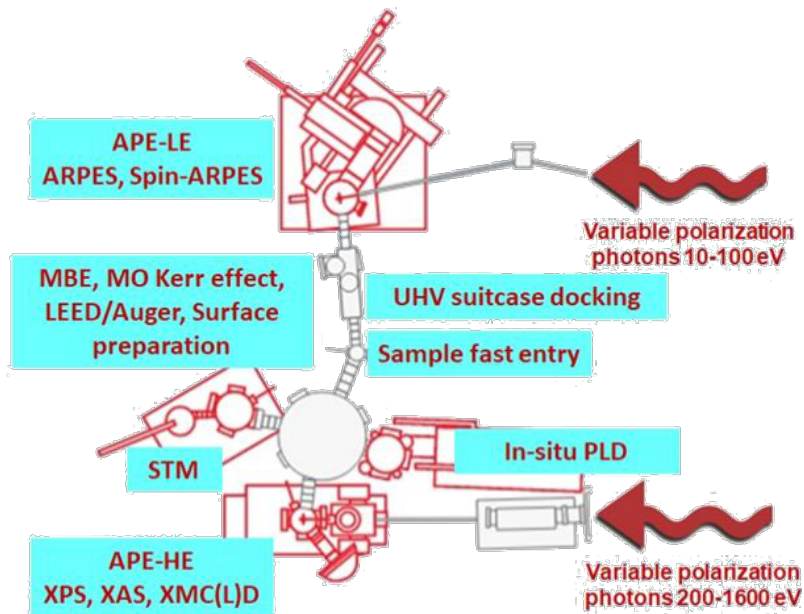


Figure 2.15: Scheme of APE beamline at Elettra synchrotron facility in Trieste. From: `https://www.elettra.trieste.it/lightsources/elettra/elettra-beamlines/ape/description.html`

## 2.7.    Sample Preparation

The preparation of samples in surface physics is a very delicate stage due to the instability of these systems. As explained earlier, UHV conditions are of crucial importance in order to have very clean surfaces; for this reason, the sample preparation is performed *in situ*. The sample preparation process is divided into two main stages: the surface cleaning process, which consists in sputtering and annealing cycles; the growth of thin films, performed via Molecular Beam Epitaxy (MBE).

### 2.7.1.    Sputtering and Annealing

During the sputtering and annealing phase, a clean and well-ordered surface is obtained. The sputtering process consists in bombarding the surface with accelerated noble gas ions, generally Ar. To do so, Ar gas is injected into the chamber through an ion gun, then the atoms are ionized because of electron collision. The electrons travel in helical trajectories due to the presence of a magnet. The exit of the ion gun is kept at a high voltage (1.5 keV in STM laboratory) to accelerate the ions onto the sample, which is grounded. When this ion beam collides with the sample, the atoms on the surface are dislodged; with this process it is possible to remove contaminants from the surface, but at the same time the quality of the surface in terms of flatness and ordering is very poor. Annealing cycles are performed to overcome this limitation. During the annealing procedure, the sample is heated up to a certain temperature (which depends on the system) for a certain amount of time. In the case of the STM laboratory, a ceramic heater heats the sample by making a current flow through it, while the temperature is measured through a thermocouple. The high temperature favours the surface atoms' mobility and it makes it possible to recover the surface order.

### 2.7.2.    Molecular Beam Epitaxy (MBE)

Molecular Beam Epitaxy is a technique that allows the growth of epitaxial thin films on substrates and it is based on the sublimation of pure materials. Thin films are very much affected by the type of substrate they are interacting with, and this can give rise to very interesting properties.

The evaporation cell for MBE is made of a rod of pure material with a filament that passes close to it. When a current passes through the filament, it starts to emit electrons by thermionic effect. These electrons can be accelerated by a high voltage (up to 2.5 keV) to induce the sublimation of the rod. This atomic beam passes through a small shutter (of diameter $\simeq 0.5$ cm) to obtain a focused beam. It is also possible to perform MBE

in an oxygen environment to grow oxide species of metallic materials. This process is called reactive deposition and it will be employed in the next chapter for chromium oxide growth.

The deposition rate of the process can be calibrated by using a quartz microbalance. The working principle is based on the shift of the quartz piezoelectric response, which is proportional to the square root of the mass of deposited material. With this instrument, it is possible to achieve sub-monolayer precision.

# 3 | Experimental Results: Growth of $Cr_2O_3$ on Cu(111) and on Cu(110) and growth of FePc on $Cr_2O_3$/Cu(110)

This chapter is dedicated to the presentation of the experimental results and it is divided into two main parts. The first one covers the growth of chromium oxide on two different copper substrates, namely Cu(111) and Cu(110). The second part covers the growth of iron phthalocyanine (FePc) molecules on $Cr_2O_3$/Cu(110). All the techniques explained in Chapter 2 are employed to study the morphological and crystallographic properties of these systems.

## 3.1. The substrates: Cu(111) and Cu(110)

Copper is a face centered cubic (FCC) crystal with a lattice parameter $a = 3.61$ Å. As represented in Figure 3.1, the (111) and the (110) surfaces present two different atomic arrangements: atoms in the (111) surface are disposed in a hexagonal lattice with lattice parameter $b = a\sqrt{2}/2 = 2.55$ Å; the atoms in the (110) surface are disposed in a rectangular lattice with lattice parameters $c_1 = 3.61$ Å and $c_2 = a\sqrt{2}/2 = 2.55$ Å.

As a first step, both the Cu(111) and the Cu(110) substrates were cleaned by numerous cycles of sputtering (performed at 480°C, $I_{Ar^+} = 15$ $\mu A$, $\Delta t = 40'$), followed by annealing at 480°C for $\Delta t = 15'$. This procedure, as mentioned in Section 2.7.1, allows to obtain a surface that is well-ordered and as free from contaminants as possible. LEED and Auger measurements were performed to check the quality of the surface in terms of both crystallographic quality and the presence of contaminants.

Figure 3.2 shows the LEED images and the Auger spectra that were obtained for the two substrates. The LEED patterns obtained in these two cases confirm the hexagonal arrangement of surface atoms of Cu(111) and the rectangular one of Cu(110) as depicted
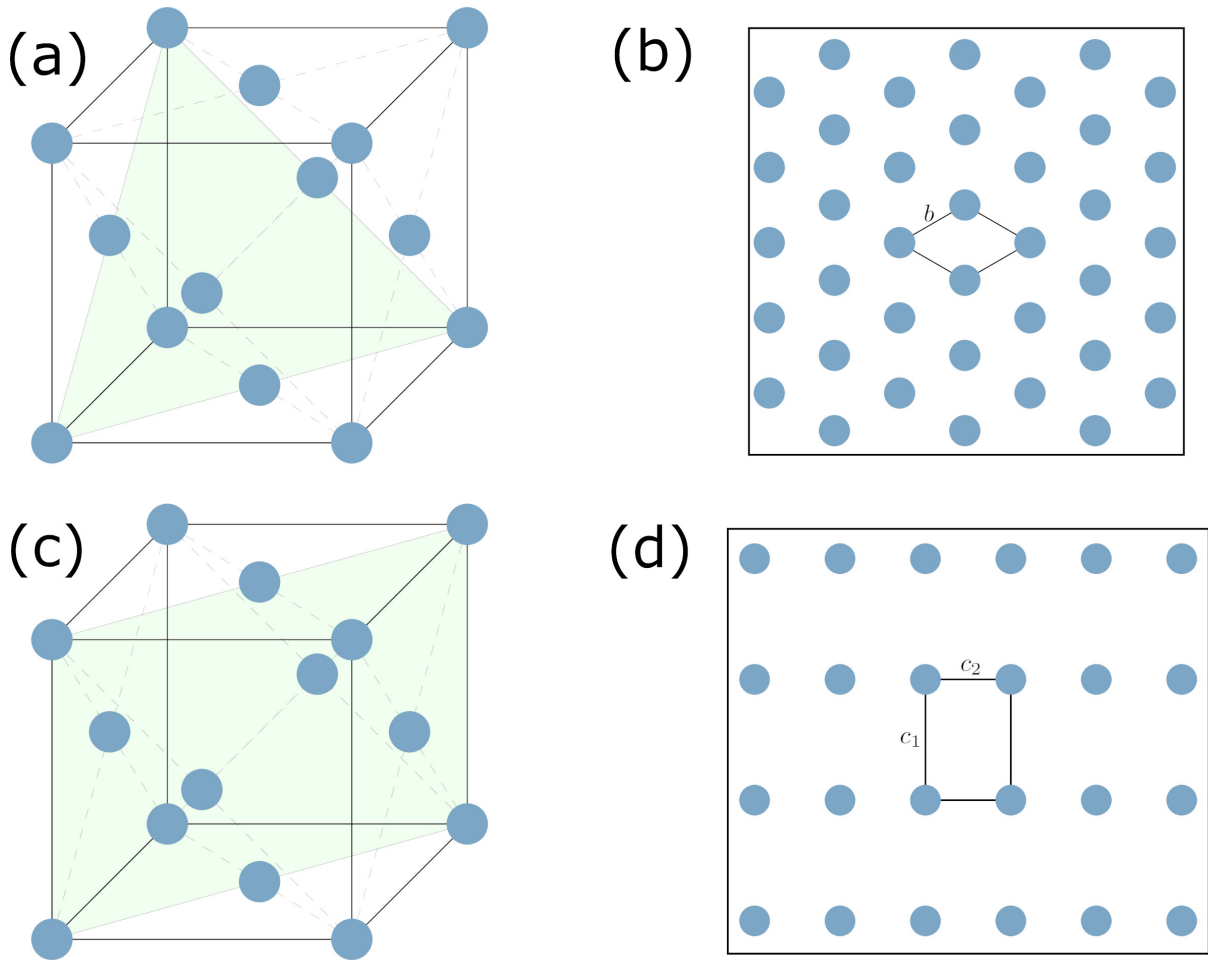
Figure 3.1: FCC structure of copper. (a) (111) plane; (b) Cu(111) surface atomic structure; (c) (110) plane; (d) Cu(110) surface atomic structure, the unit cell is highlighted in black.

in Figures 3.1(b) for Cu(111) and 3.1(d) for Cu(110).

In addition, STM images of the substrates were acquired in order to check the morphology of the surfaces. Two large-scale ($350 \times 350$ nm$^2$) images of Cu(110) and Cu(111) are reported in Figure 3.3, where it is possible to see that both samples show surfaces with flat terraces for relatively large areas (beyond 200 nm), which are separated by small steps of constant height, around 0.1 nm for Cu(110) and 0.2 nm for Cu(111).

# Cu(111)     Cu(110)
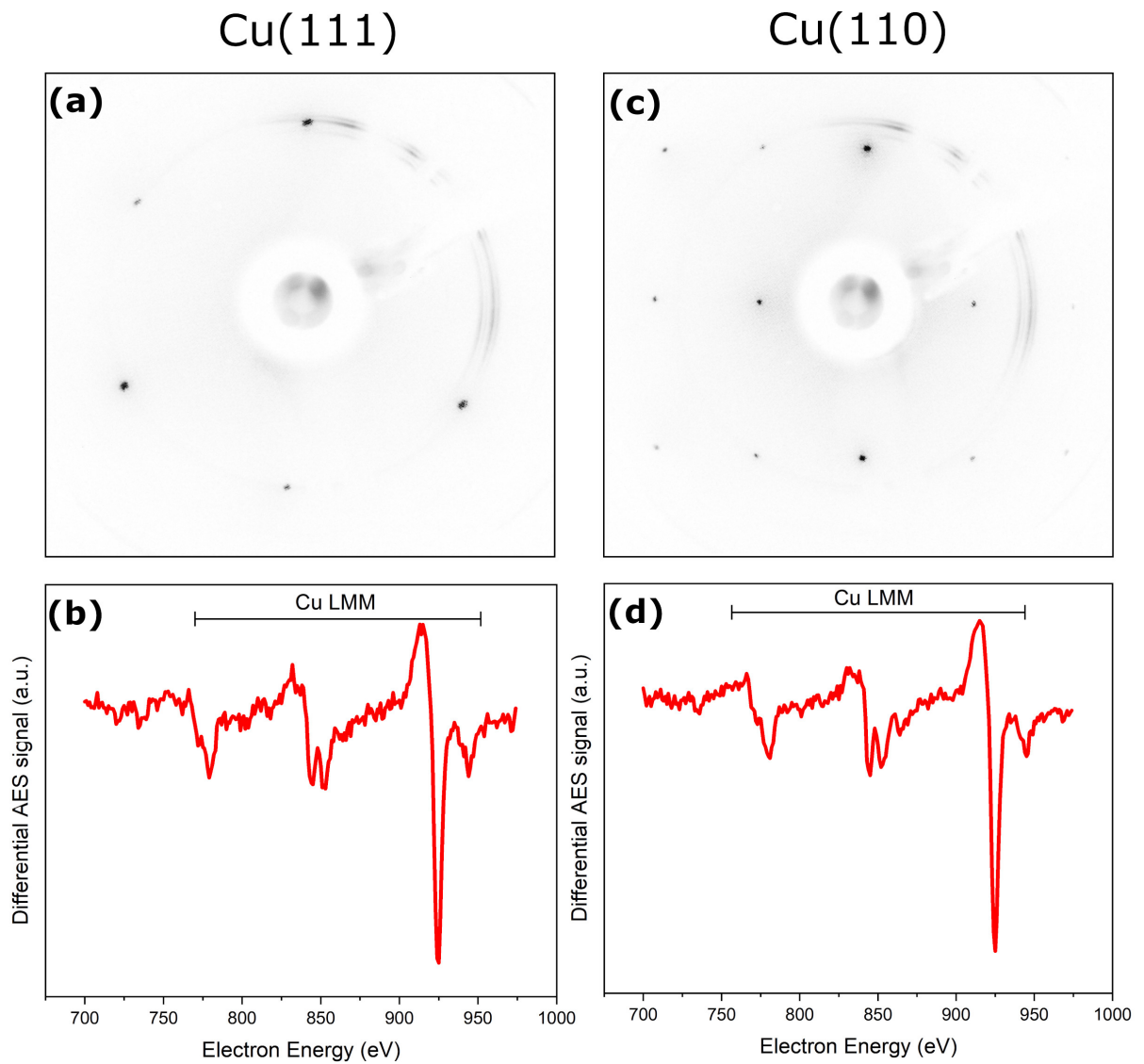


Figure 3.2: (a) LEED pattern of Cu(111), 150 eV; (b) AES of Cu LMM levels measured from the Cu(111) sample, beam energy 3 keV; (c) LEED pattern of Cu(110), 150 eV; (d) AES of Cu LMM levels measured from the Cu(110) sample, beam energy 3 keV.

Cu(110)                                          Cu(111)
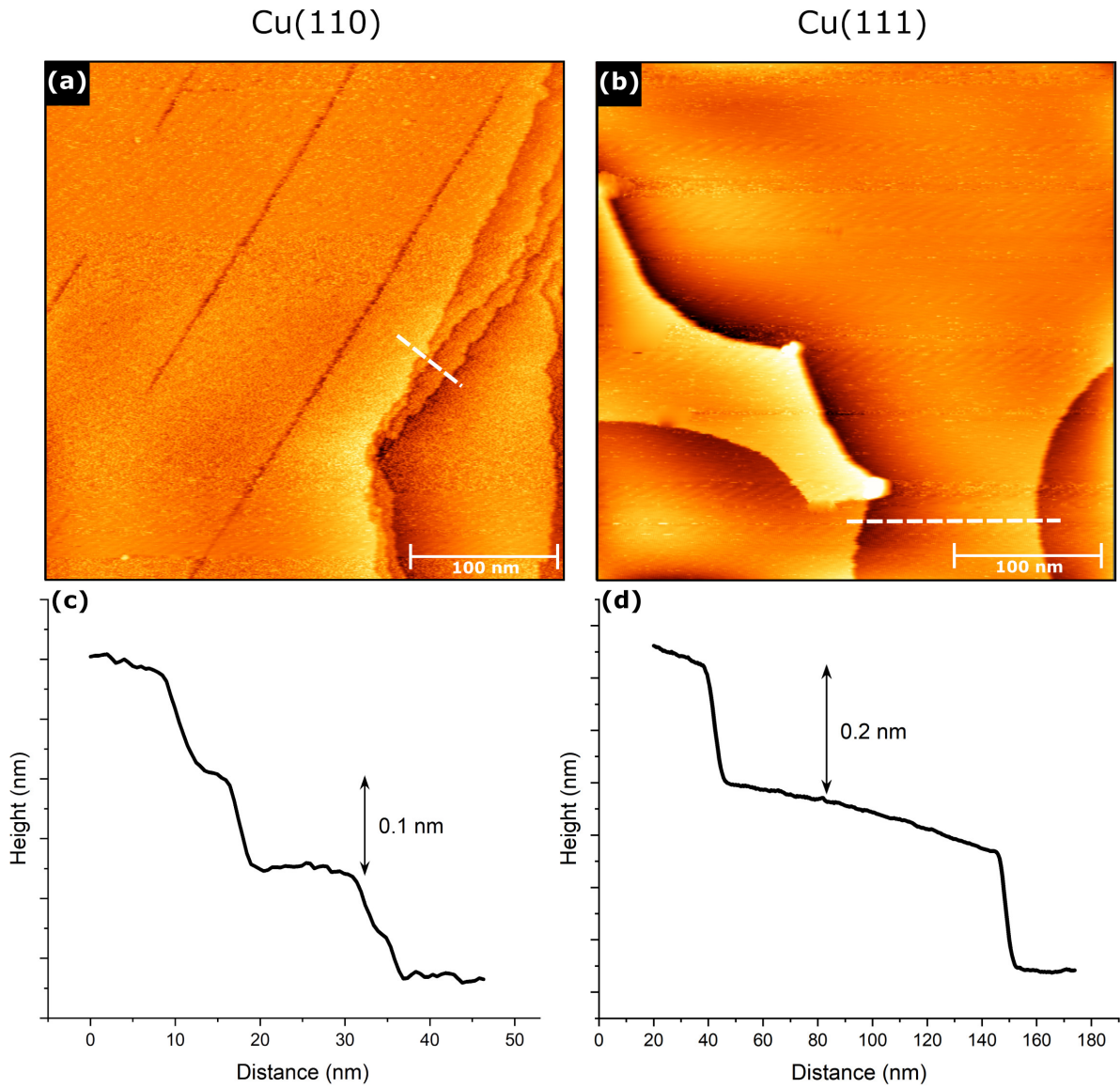


Figure 3.3: STM images ($350 \times 350$ nm$^2$) of Cu(110) and Cu(111): (a) Cu(110) with topographical curve (c) corresponding to white line drawn on panel (a), $\Delta V = 0.1$ V, $I = 2$ nA. (b) Cu(111) with topographical curve (d) corresponding to white line drawn on panel (b), $\Delta V = 0.1$ V, $I = 1$ nA.

## 3.2. Growth of $Cr_2O_3$ on Cu(111) and Cu(110)

This section deals with the characterization of the growth of chromium oxide, $Cr_2O_3$, on two different substrates, Cu(110) and Cu(111). Chromium oxide films of different thicknesses were grown on these substrates to study the growth evolution of the oxide.

### 3.2.1. Study of the growth of $Cr_2O_3$ on Cu(110)

After the cleaning process, it was possible to deposit chromium oxide on Cu(110). The deposition was performed by reactive deposition (see Section 2.7.2) at $T = 435°$ C in oxygen environment at $p_{O_2} = 10^{-6}$ mbar, followed by an annealing at $T = 435°$ C, $p_{O_2} = 10^{-6}$ mbar, for $\Delta t = 1'$.

Auger spectra were taken to check the chemical composition and thickness of $Cr_2O_3$: Figure 3.4 compares the AES signal of Cu for different thicknesses of chromium oxide films. The AES peaks of Cu are attenuated as the $Cr_2O_3$ film grows thicker. The attenuation of the intensity of AES peaks of the substrate as a result of the deposition of a thin film follows the Lambert-Beer law: $I = I_0 \exp\left(-\frac{d}{\lambda}\right)$, where $I_0$ is the original intensity of the peak, $d$ is the thickness of the film and $\lambda$ is the inelastic mean free path of the electrons. From the Auger spectra, it is therefore possible to give a very rough estimation of the thickness $d$ of the deposited film. Figure 3.5 shows the AES peaks of chromium and oxygen for different thicknesses of chromium oxide, starting from the clean substrate and up to 1.2 nm of $Cr_2O_3$. The Auger signal of Cr and O is obviously increasing for thicker $Cr_2O_3$ films.
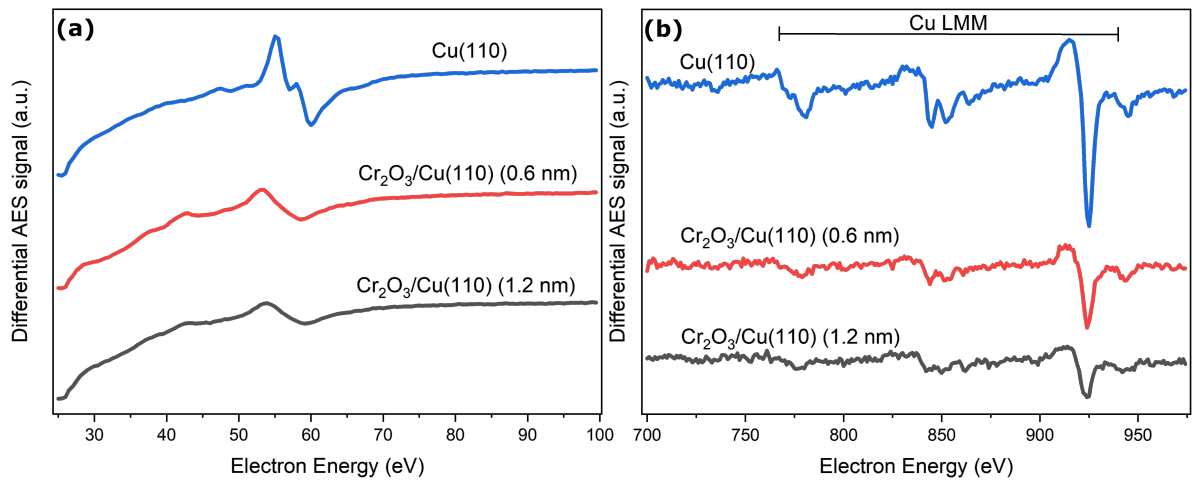


Figure 3.4: (a) Low energy AES of Cu for different $Cr_2O_3$ thicknesses, beam energy 3 keV. (b) AES of Cu LMM for different $Cr_2O_3$ thicknesses, beam energy 3 keV. Cu peaks are attenuated as the $Cr_2O_3$ becomes thicker.
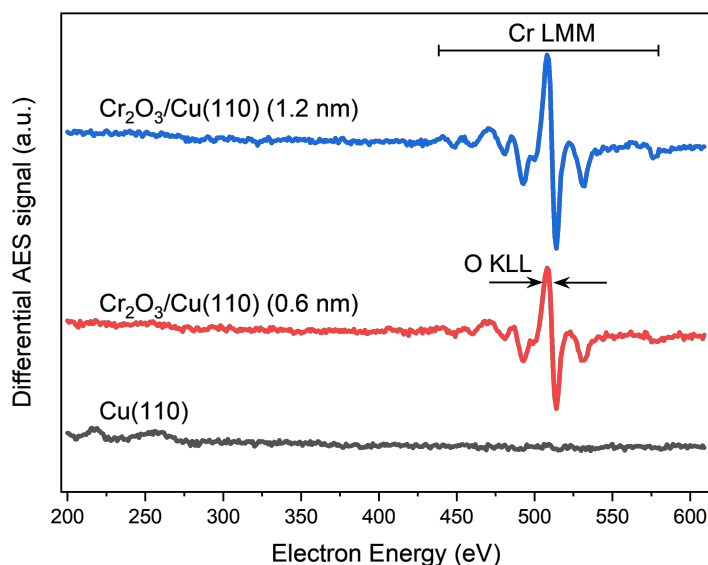
Figure 3.5: AES of Cr LMM and O KLL for different thicknesses of chromium oxide, from the clean substrate to 1.2 nm of $Cr_2O_3$, beam energy 3 keV.

From AES it could be also possible to estimate the stoichiometry of the oxide, by looking at the Cr/O peaks ratio. Unfortunately, the peaks of Cr and O are superimposed, which makes this type of estimation unreliable in this case. The LEED images are reported in Figure 3.6 for oxide thicknesses of 0.6 nm and 1.2 nm. In both Figure 3.6(a) and 3.6(b), the LEED pattern shows two hexagons that are rotated by 30° with respect two each other; also, in both patterns there is one hexagon that appears to be brighter than the other. From this, one can argue that chromium oxide grows in two hexagonal domains that are rotated by 30° and that there is one domain that appears to be more long-range ordered than the other.
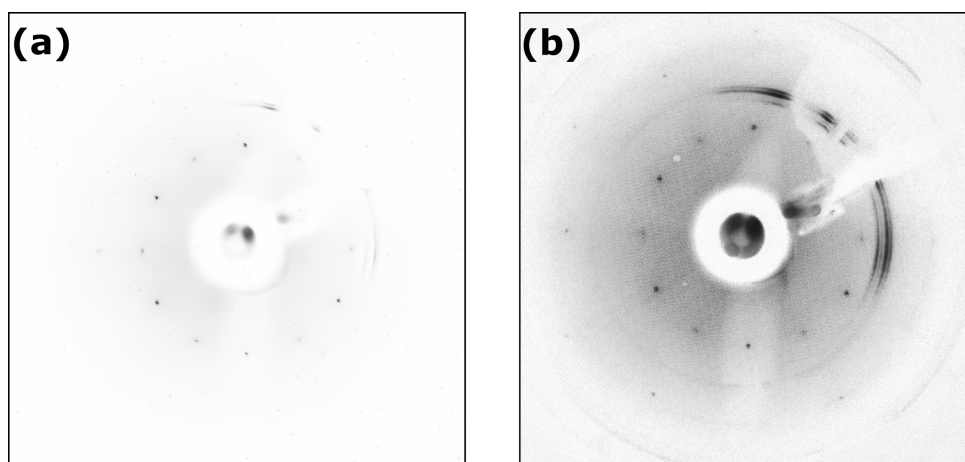


Figure 3.6: (a) LEED image of 0.6 nm of $Cr_2O_3$/Cu(110), 200 eV. (b) LEED image of 1.2 nm of $Cr_2O_3$/Cu(110), 200 eV.

Several STM images of this system were taken in order to study the morphology of the surface for different coverage of chromium oxide. In Figure 3.7(a) the surface morphology for 0.3 nm of $Cr_2O_3$ is shown. It appears that chromium oxide forms atomically flat islands with a constant height of 1 nm (which corresponds to a single $Cr_2O_3$ cell). The elongated islands that are visible in Figure 3.7(a) are likely responsible for the less-intense LEED domain. Upon increasing the coverage to 0.45 nm (Figure 3.7(c)), we can notice that the islands become larger while keeping the same thickness of 1 nm, but at the same time, a new layer starts to form on top of the islands. The thickness of this new layer appears to be 0.5 nm, around half the oxide cell. This tendency is even more evident by increasing the oxide thickness to 0.6 nm (Figure 3.7(e)): here we can see that both the two layers are still clearly visible, while the terraces are generally larger. This suggests the possibility of saturating the surface completely, and in fact, by raising the oxide thickness to 1.2 nm the sample appeared to be totally covered by the oxide. However, the system was too insulating to obtain a good STM image.
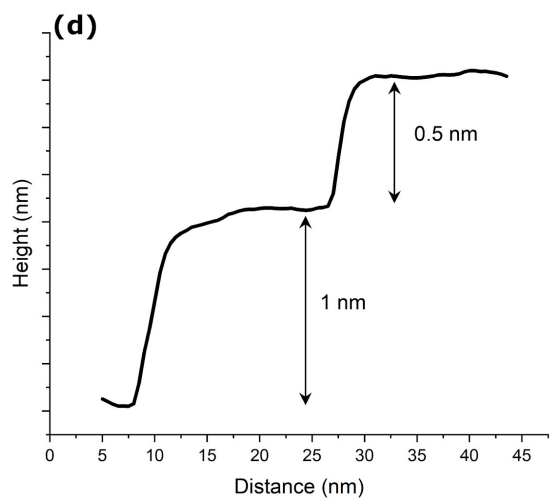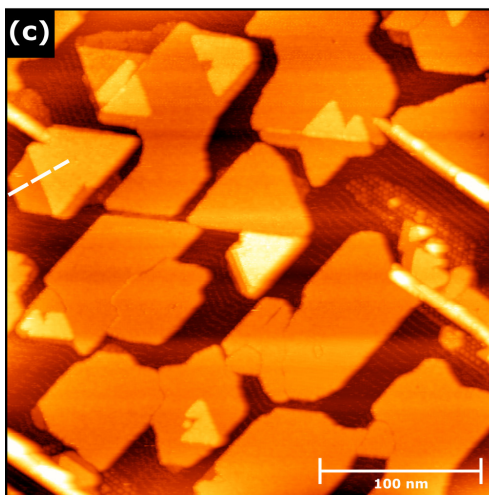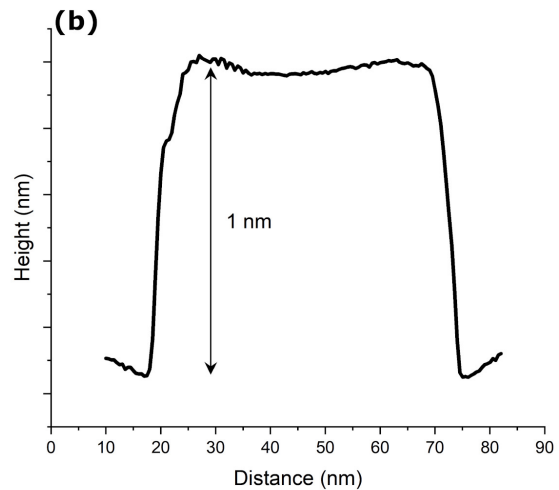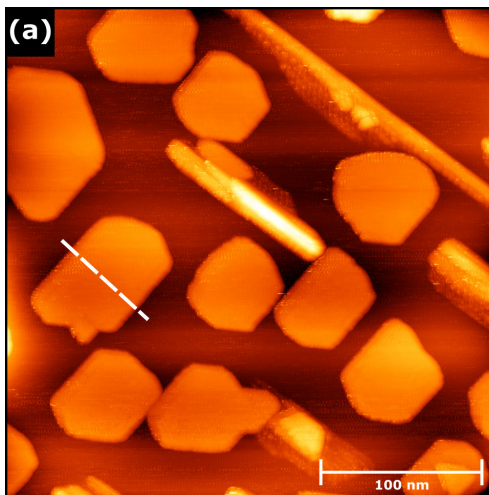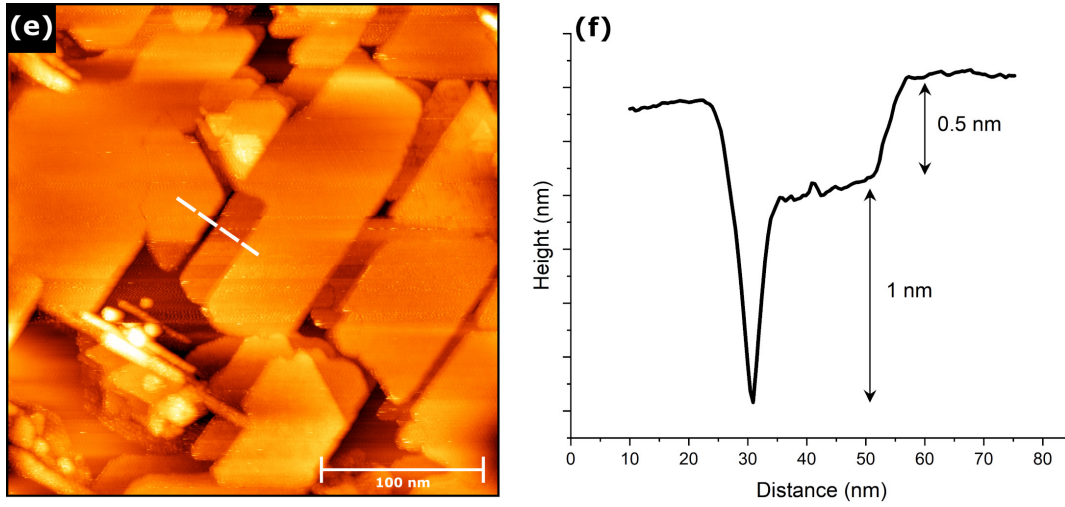
Figure 3.7: STM images ($300 \times 300$ nm$^2$) of Cr$_2$O$_3$/Cu(110). (a) 0.3 nm thickness, $\Delta V = -2$ V, $I = 0.5$ nA; (b) topographical curve corresponding to white line drawn on panel (a); (c) 0.45 nm thickness thickness, $\Delta V = -1.8$ V, $I = 0.5$ nA; (d) topographical curve corresponding to white line drawn on panel (c); (e) 0.6 nm thickness thickness, $\Delta V = -2$ V, $I = 0.5$ nA; (f) topographical curve corresponding to white line drawn on panel (e).

### 3.2.2.  Study of the growth of Cr$_2$O$_3$ on Cu(111)

The growth of chromium oxide has been studied on Cu(111) as well. The steps followed in this process are the same as the ones of Cr$_2$O$_3$/Cu(110): after the cleaning of the surface by sputtering and annealing cycles, the oxide was deposited via reactive deposition at $T = 435°$ C in oxygen environment at $p_{O_2} = 10^{-6}$ mbar, followed by an annealing at $T = 435°$ C, $p_{O_2} = 10^{-6}$ mbar, for $\Delta t = 1'$.

Like in the previous Section, the growth of chromium oxide was checked with Auger Electron Spectroscopy and Low Energy Electron diffraction. Figure 3.8 shows the Auger spectra of Cr$_2$O$_3$ for coverage of 0.6 nm and 1.2 nm; as expected, the AES signal looks identical to the one of Cr$_2$O$_3$/Cu(110) of Figure 3.5, indicating that the chemical composition is the same.

The LEED pattern of Cr$_2$O$_3$/Cu(111) is represented in Figure 3.9: a single hexagonal pattern is visible, in contrast with the double hexagonal pattern of Cr$_2$O$_3$/Cu(110) of Figure 3.6. Also, the LEED pattern Cr$_2$O$_3$/Cu(111) shows double spots: the inner ones are related to the chromium oxide, while the outer one are related to the substrate, which also has an hexagonal LEED pattern (see Figure 3.2(a)).
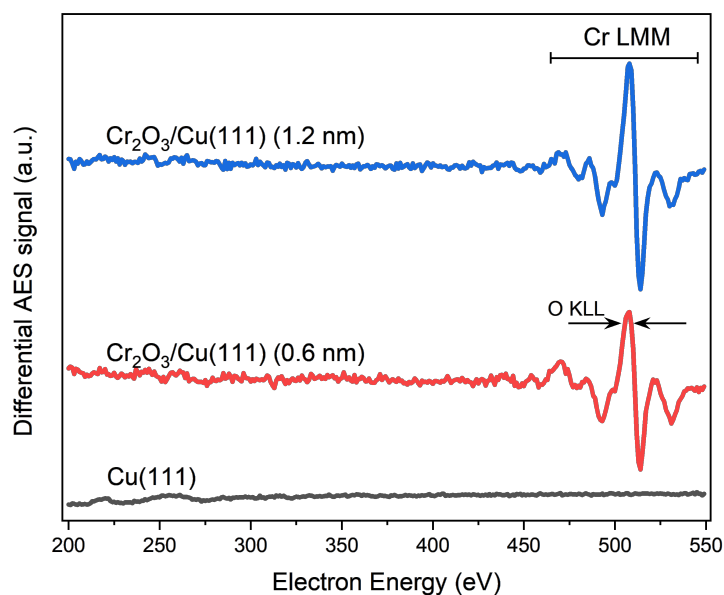
Figure 3.8: AES of Cr LMM and O KLL for different thicknesses of chromium oxide, from the clean substrate to 1.2 nm of $Cr_2O_3$, beam energy 3 keV.
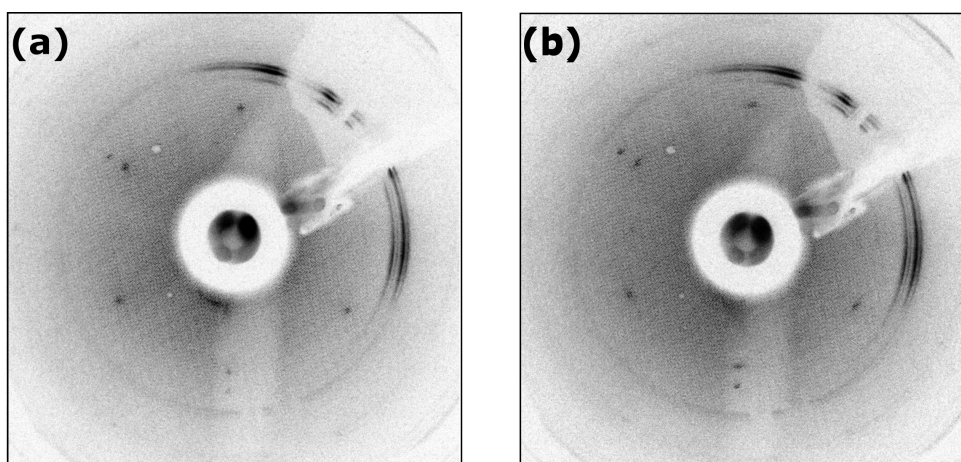


Figure 3.9: LEED patterns of $Cr_2O_3/Cu(111)$. (a) 0.6 nm, 200 eV; (b) 1.2 nm, 200 eV.

The STM images for $Cr_2O_3/Cu(111)$ are reported in Figure 3.10. The surface for coverage of 0.6 nm appears similar to the one of $Cr_2O_3/Cu(110)$ in Figure 3.7(a), with 1 nm high islands. However, for coverage of 1.2 nm, the islands do not seem to merge anymore, but instead they seem to grow higher. Islands with heights of around 2-2.5 nm have been observed, and they appear to be separated by large regions of clean Cu. Given the impossibility to saturate the surface with this coverage, it has been decided to grow the FePc molecular layer only on $Cr_2O_3/Cu(110)$.
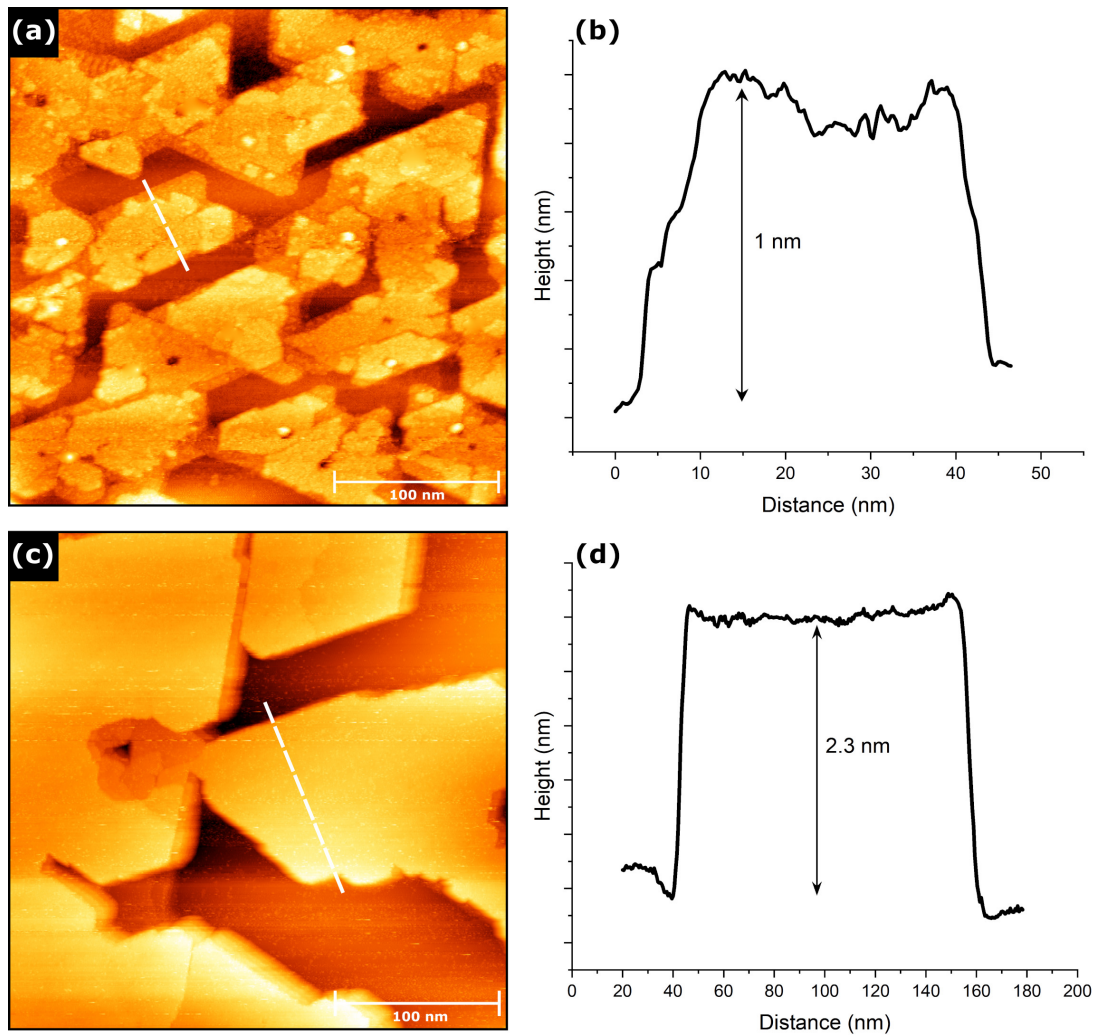
Figure 3.10: STM images $(300 \times 300 \text{ nm}^2)$ of $Cr_2O_3/Cu(111)$: (a) 0.6 nm of chromium oxide, $\Delta V = -1.8$ V, $I = 0.4$ nA; (b) topographical curve corresponding to white line drawn on panel (a); (c) 1.2 nm of chromium oxide, $\Delta V = -3.3$ V, $I = 0.2$ nA; (d) topographical curve corresponding to white line drawn on panel (c).

### 3.2.3.   Oxide stoichiometry

Up until now, the stoichiometry of chromium oxide was simply assumed to be $Cr_2O_3$. However, $Cr_2O_3$ is not the only possible type of chromium oxide: the other possible oxides are $CrO$, $CrO_2$ and $CrO_3$. In order to determine the oxidation state of Cr, X-Ray Absorption Spectroscopy (XAS) has been performed on the chromium oxide film on Cu(110). As mentioned in Section 2.5.1, XAS is a spectroscopic technique that can give insights into the chemical environment of atoms. In this case, the focus is on the oxidation state of Cr.

XAS measurements were performed at Elettra synchrotron facility in Trieste. The sample was prepared *in situ* following the same exact recipe that was presented in the previous section. XAS was performed at the $L_{2,3}$ edges (corresponding to the $2p_{1/2}$ and $2p_{3/2}$ ) of Cr. The result is shown in Figure 3.11 for a 1.2 nm thick chromium oxide film on Cu(110). The XAS spectra corresponding to $CrO$, $CrO_2$, $CrO_3$, and $Cr_2O_3$ are reported next to the experimental spectrum and they are obtained from literature [41]. Obviously, there is no XAS signal for the clean Cu(110) (red curve). This is useful for checking if the substrate has been properly cleaned by sputtering/annealing cycles before starting the deposition. The similarity of the experimental XAS spectrum with the reference spectrum of $Cr_2O_3$ is evident and it confirms that Cr atoms are in a +3 oxidation state, therefore the chromium oxide film grown on Cu(110) is indeed $Cr_2O_3$. The other spectra corresponding to different oxidation states of Cr can be easily ruled out.
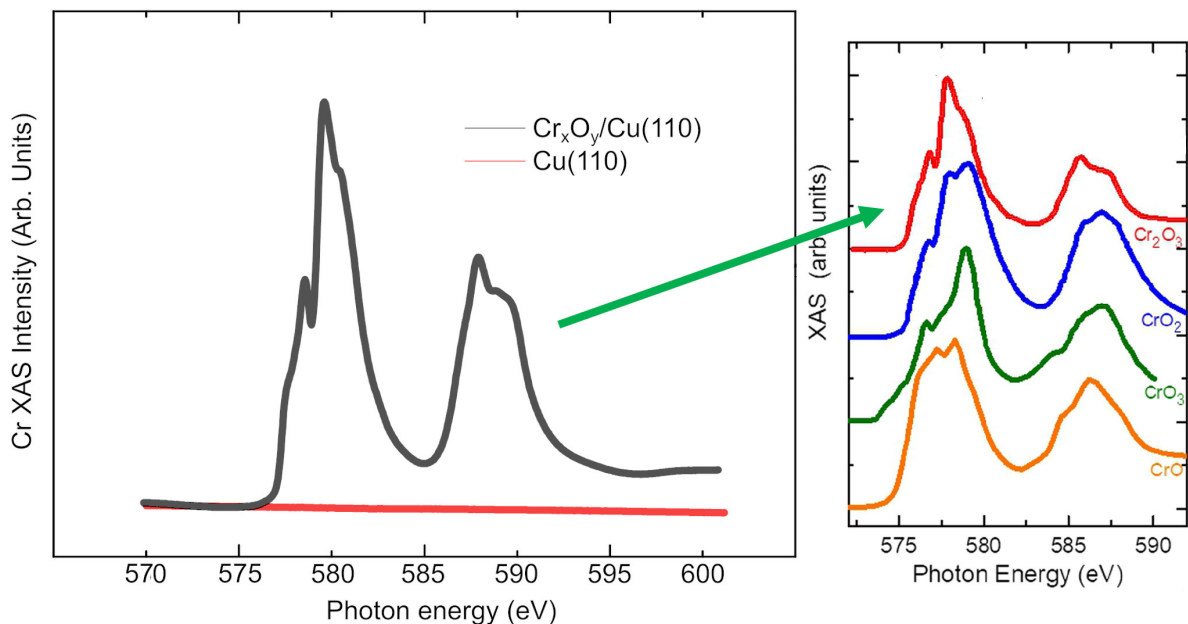


Figure 3.11: XAS of $L_{2,3}$ edges of Cr, with references of different spectra for different oxidation states of Cr [41].

## 3.2.4. Model of growth of $Cr_2O_3/Cu(110)$

The lattice parameter of chromium oxide can be estimated from the LEED pattern. Figure 3.12 shows the LEED pattern of $Cr_2O_3$ with the LEED pattern of Cu(110) superimposed (light blue dots). By the comparison of the LEED pattern before and after the deposition, it is possible to give a rough estimation of $a_{ox}$:

$$a_2 \simeq b \rightarrow \frac{2\pi}{a_{Cu}} \simeq \frac{2\pi}{a_{ox}\sin\frac{\pi}{3}} \rightarrow a_{ox} \simeq \frac{2}{\sqrt{3}}a_{Cu} = 2.95 \text{ Å} \qquad (3.1)$$

This result for the lattice parameter is rather distant from the 4.96 Å of bulk-terminated $Cr_2O_3(0001)$ surface. In fact, it is much closer to the lattice parameter of the oxygen sublattice in $Cr_2O_3$, which is $a_O = 2.86$ Å: this suggests that the chromium oxide film may present a surface with an oxygen-rich termination.
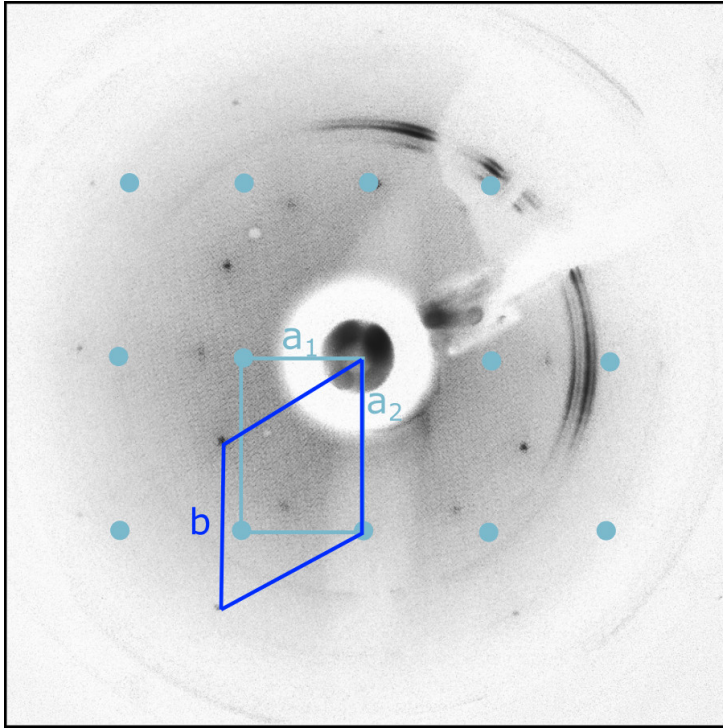


Figure 3.12: LEED pattern of $Cr_2O_3$ with superimposed the Cu(110) LEED pattern.

The oxygen-rich termination is one of the three possible surface terminations of $Cr_2O_3$, as it was discussed in Section 1.4.2. This type of surface termination, however, does not account for the hexagonal structure.

A possible explaination is that the chromium oxide surface undergoes a CrO surface reconstruction. Such reconstruction is depicted in Figure 3.13(a), where it is possible to see from the side view that the CrO reconstruction can be thought as a bulk-terminated $Cr_2O_3$

in which the Cr hexagons intercalated below the oxygen. With this surface reconstruction, the hexagonal structure is retrieved, as represented in Figure 3.13(b).
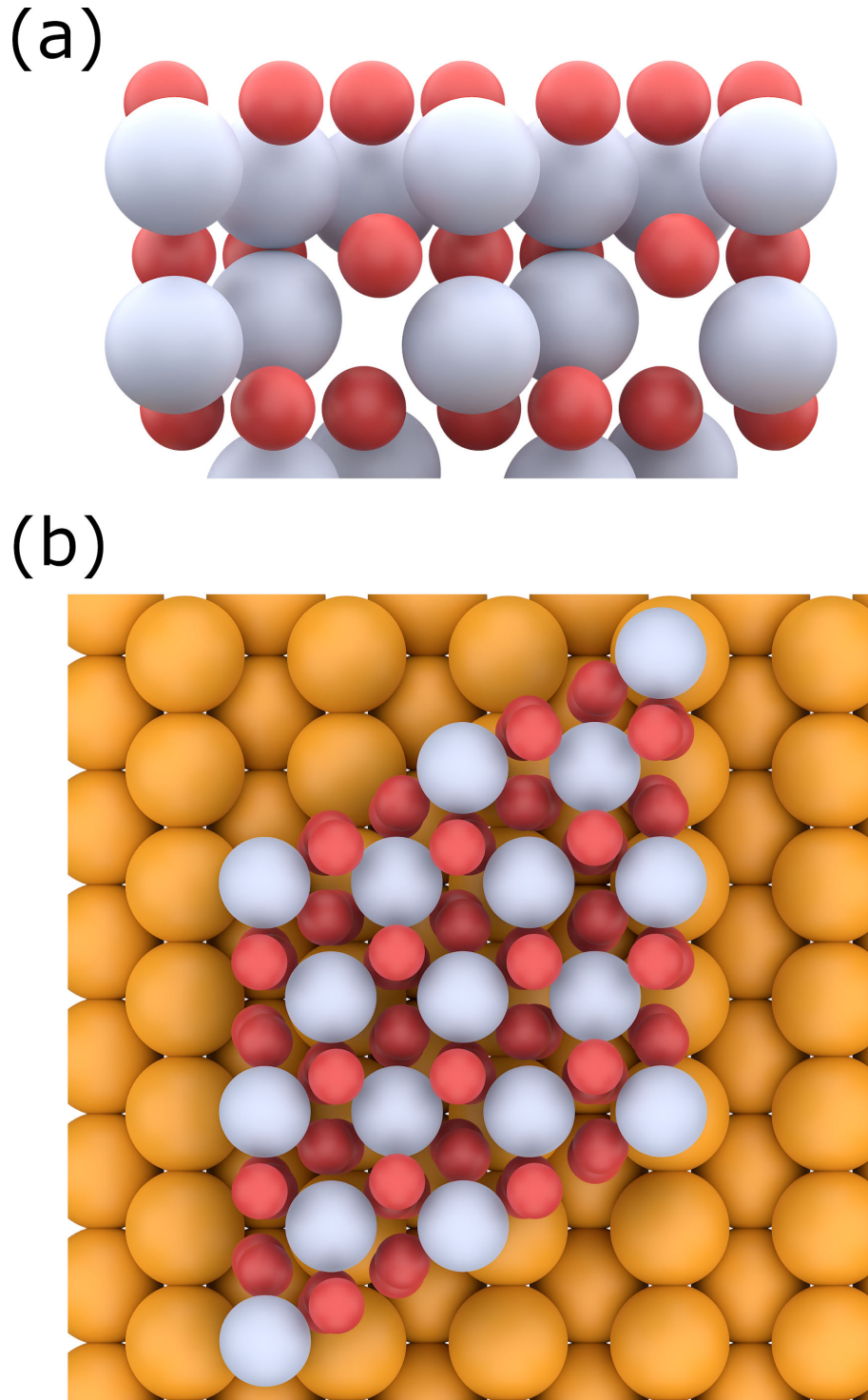


Figure 3.13: Growth structure of $Cr_2O_3$ on Cu(110); (a) side view of CrO reconstruction; (b) top view of hexagonal chromium oxide surface.

## 3.3.   Growth of FePc on $Cr_2O_3$/Cu(110)

This section covers the study of the growth of iron phthalocyanine molecules (FePcs) on $Cr_2O_3$/Cu(110). It is divided in two parts: in the first one, the deposition of FePcs on bare Cu(110) will be presented; the second part will deal with the deposition of FePcs on $Cr_2O_3$/Cu(110).

### 3.3.1.   Study of the growth of FePc on Cu(110)

The deposition of iron phthalocyanine (FePc) molecules on clean Cu(110) was performed before the deposition on chromium oxide to see if it was possible to obtain an ordered layer on the metallic surface. The adsorption properties of FePc molecules have already been investigated in scientific literature on metal substrates such as Ag(110) [42], Au(110) [43] and also Cu(110) [44]. These works have shown that it is possible to obtain ordered structures of FePc molecules on clean metal surfaces; in the case of Cu(110), the most stable configuration for the adsorption of FePc on Cu(110) is that on the top site of Cu with an angle of 45° between the lobe of the molecule and the [110] direction.
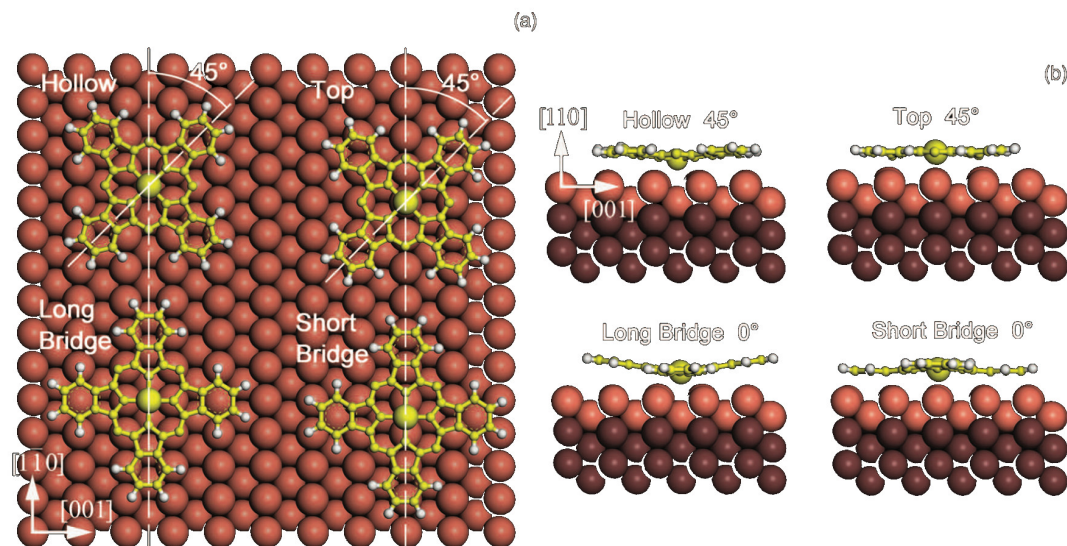


Figure 3.14: Different adsorption geometries of FePc on Cu(110), the top site configuration is the most stable. Reprinted from [44].

FePc molecules were deposited by MBE on Cu(110) at room temperature after cleaning the substrate with cycles of sputtering and annealing. The morphology of the surface was studied as usual with STM. Figure 3.15 shows that FePc molecules indeed tend to form

an ordered layer on a clean Cu(110) surface. Two rotated square domains are visible in Figure 3.15(a), from which it is also possible to see that deposition coverage is in the sub-monolayer range. Zooming in to one of these domains shows that the molecules arrange in a square lattice with a parameter of 1.8 nm, also the orientation of the lobes seems consistent with what is already known by literature (see Figure 3.14).

Despite forming an ordered layer, it was not possible to observe a LEED pattern. The main reason is that the LEED signal produced by this sub-monolayer system is not strong enough to be observed with the LEED setup available at the STM laboratory. Another factor that makes it difficult to observe this LEED pattern is that the electron beam can cause the desorption of molecules from the substrate.
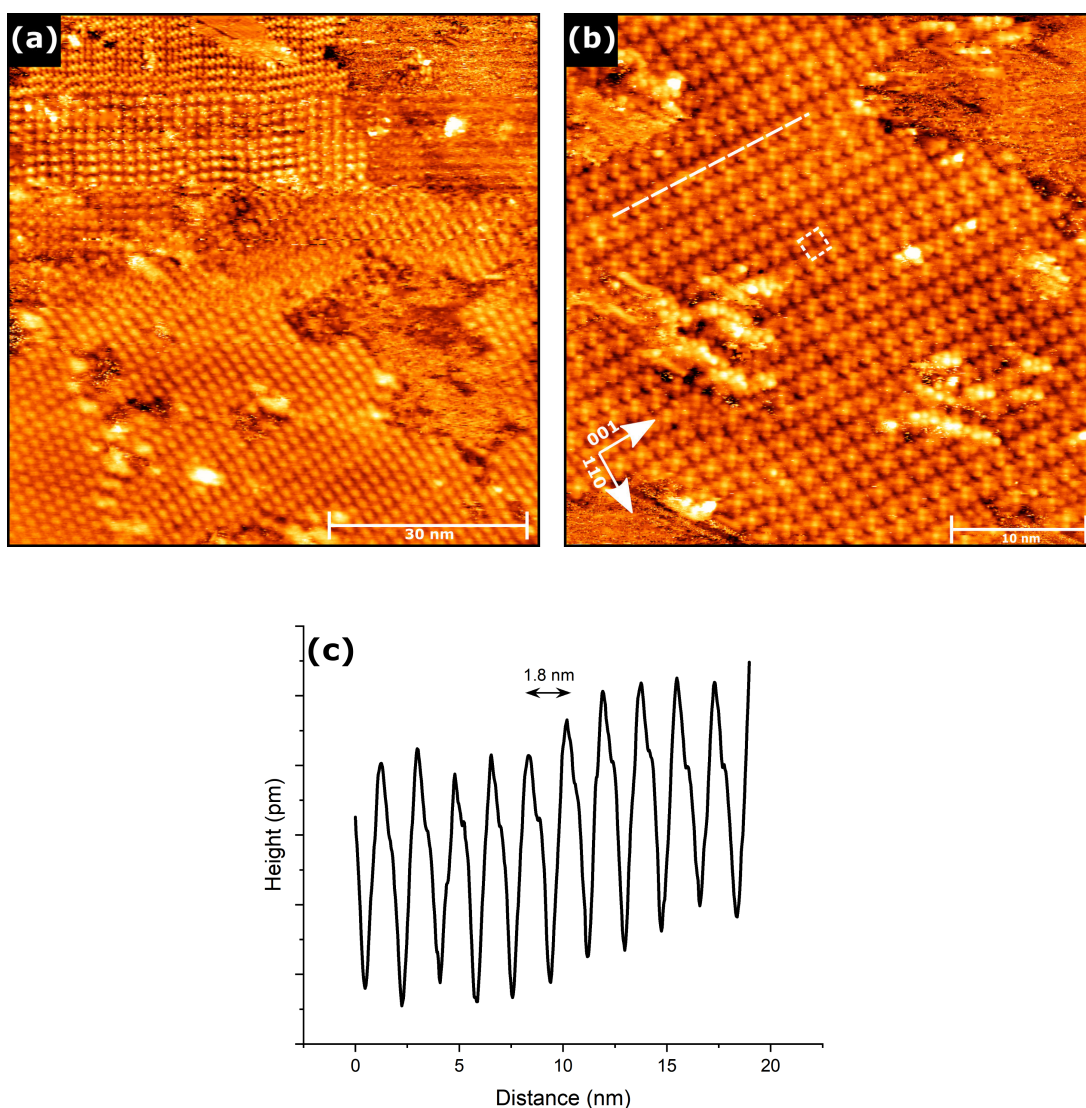


Figure 3.15: STM images of FePc/Cu(110): (a) $80 \times 80$ nm$^2$, $\Delta V = -1.8$ V, $I = 0.4$ nA; (b) $30 \times 30$ nm$^2$, $\Delta V = -1.8$ V, $I = 0.4$ nA; (c) topographical curve corresponding to white line drawn on panel (b).

### 3.3.2.   Study of the growth of FePc on $Cr_2O_3$/Cu(110)

After the characterization of the growth of chromium oxide on Cu(110), the following step was to deposit iron phthalocyanine (FePc) molecules, with the goal of obtaining a layer that is ordered both structurally and magnetically. Again, the deposition was performed via MBE at room temperature. Samples with different coverage were characterized, from sub-monolayer to full monolayer coverage.

Auger Electron Spectroscopy was employed to check if FePc molecules were successfully deposited. Figure 3.16 shows a comparison between the Auger spectra of $Cr_2O_3$/Cu(110) and FePc/$Cr_2O_3$/Cu(110). The successful deposition of FePc is confirmed by the presence of carbon and nitrogen peaks which would not be present otherwise on the clean $Cr_2O_3$/Cu(110). Also, the peaks of chromium and oxygen are attenuated due to the presence of the new organic layer on top.

As explained in Section 3.3.1, it was not possible to observe any LEED pattern related to the molecules, thus the surface morphology was studied directly with STM.
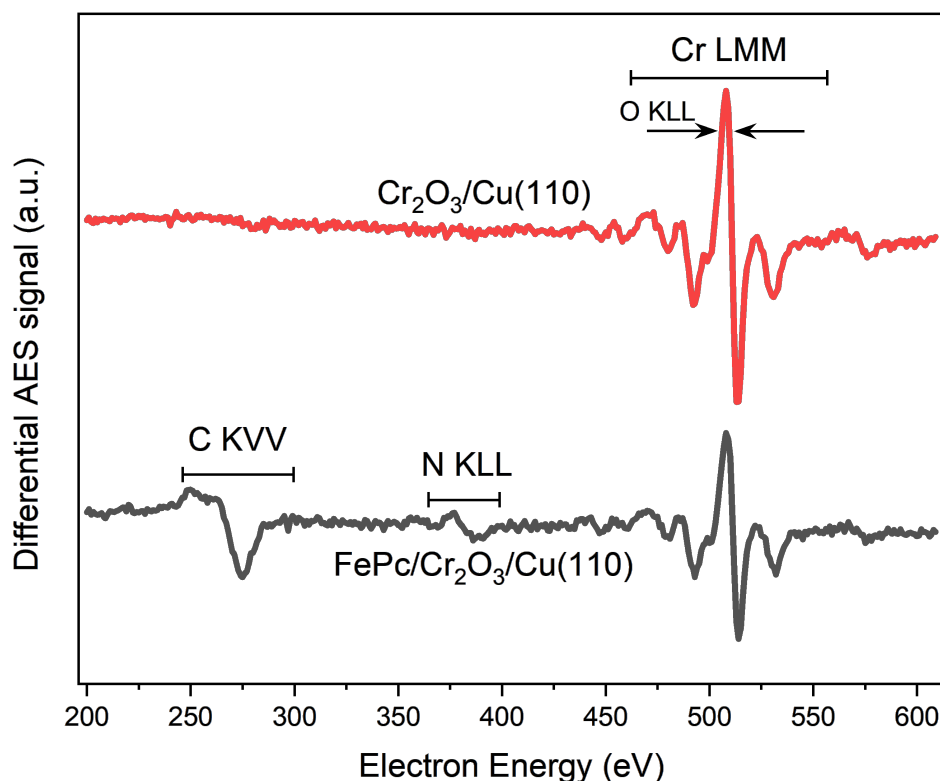


Figure 3.16:  AES of $Cr_2O_3$/Cu(110) and FePC/$Cr_2O_3$/Cu(110), beam energy 3 keV.

The first STM image in Figure 3.17 is related to a sub-monolayer coverage. Here the molecules appear to be ordered on the chromium oxide island in a hexagonal arrangement with a periodicity of 1.5 nm.
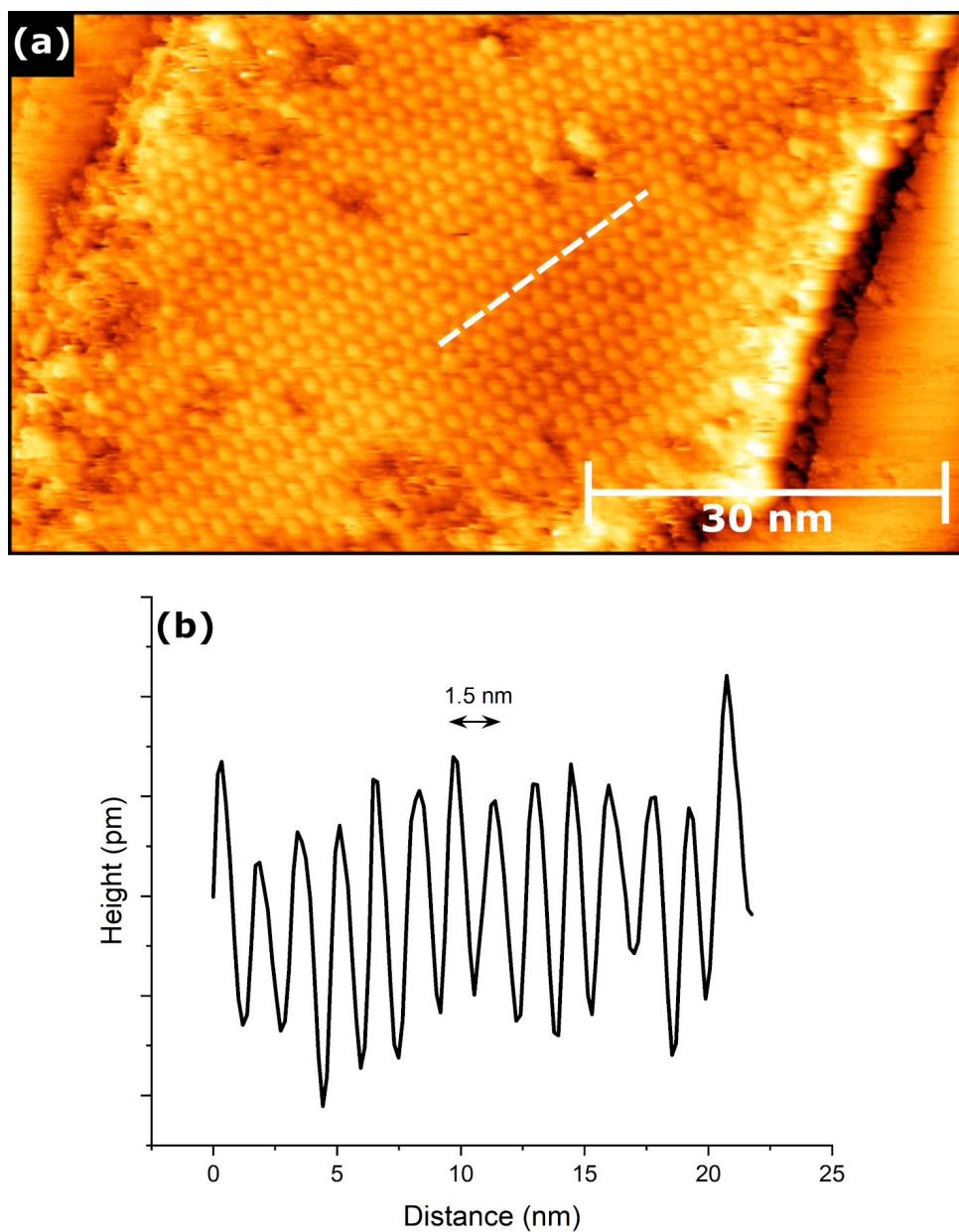
Figure 3.17: (a) STM image ($80 \times 45$ nm$^2$) of FePc/Cr$_2$O$_3$/Cu(110) with sub-monolayer coverage; $\Delta V = -1.8$ V, $I = 0.6$ nA; (b) topographical curve corresponding to white line drawn on panel (a).

The second image (Figure 3.18) shows a full monolayer coverage of FePc. In this figure, it is possible to distinguish the ordered layer on top of the metal, while the molecules on the oxide appear to be rather disordered. There are small regions on the oxide in which a short-range order of the molecules appears; this suggests annealing the sample to increase the mobility of the molecules and possibly obtain some longer-range order. Even

in this case, however, it was never possible to observe an ordered layer. Nevertheless, the molecules lie on top of the oxide with planar geometry. This fact indicates that in this system the interaction between the oxide and the molecular overlayer is rather strong: this is a non-trivial result since the interaction between molecules and oxides is usually quite weak.

A small periodicity of 0.55 nm is visible on the metal, and it is due to the $p(2 \times 1)$ surface reconstruction of oxygen on Cu: this reconstruction is formed during the reactive deposition of chromium oxide, when the Cu substrate is heated at $T = 435°$ C and it is exposed to oxygen at pressure $p_{O_2} = 10^{-6}$ mbar.
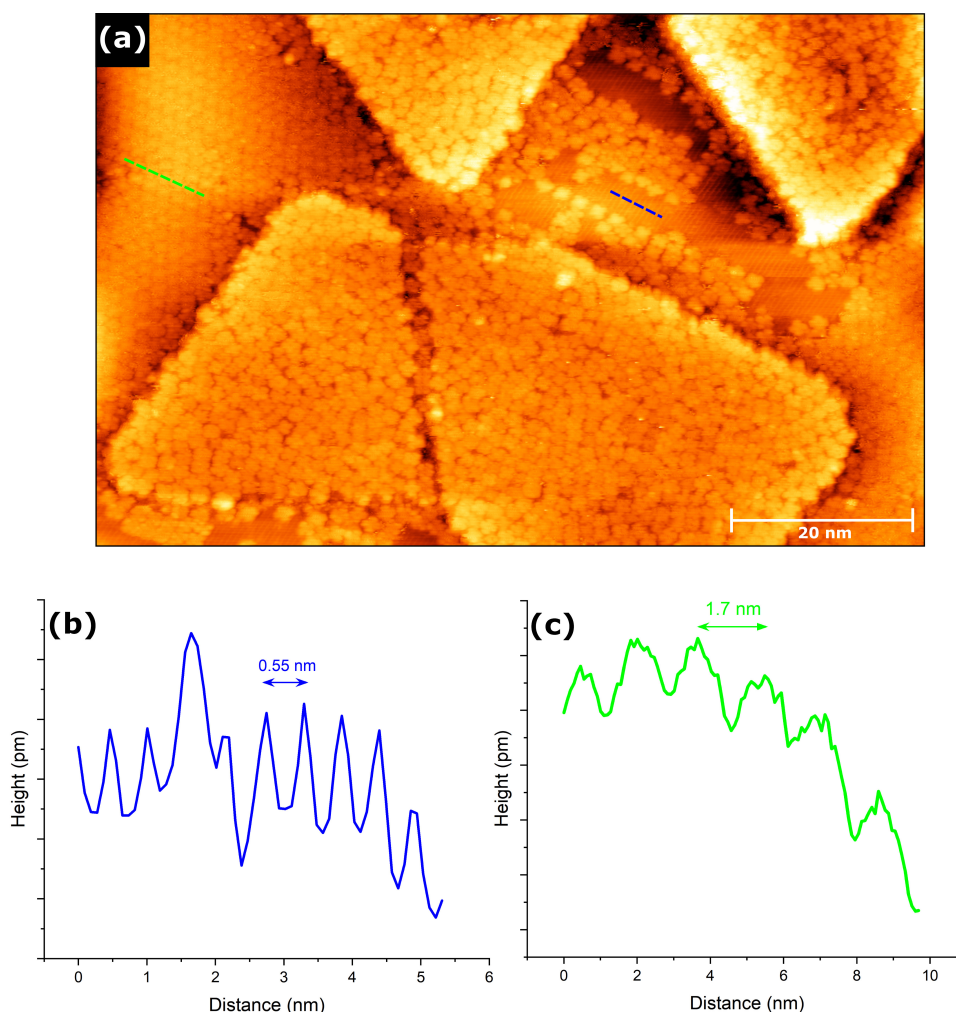


Figure 3.18: (a) STM image ($90 \times 60$ nm$^2$) of FePc/Cr$_2$O$_3$/Cu(110) with monolayer coverage; $\Delta V = -2$ V, $I = 0.6$ nA; (b) topographical curve corresponding to blue line drawn on panel (a); (c) topographical curve corresponding to green line drawn on panel (a).

### 3.3.3. XAS and XMCD of FePc/Cr$_2$O$_3$/Cu(110)

After the topographical characterization of the sample, another important aspect is the study of its magnetic properties. The possibility of obtaining a magnetically ordered organic molecular film is of great interest for potential technological application, as it was pointed out in Section 1.1.1. X-Ray Magnetic Circular Dichroism (XMCD) is the technique that was employed to study the magnetic properties of the FePc molecular layer on Cr$_2$O$_3$/Cu(110). The measurements were performed at Elettra Synchrotron Facility in Trieste, at Ape-HE beamline.

The sample was prepared *in situ*, following the same recipes that were used in the previous sections. Cu(110) substrate was cleaned by sputtering and annealing cycles, chromium oxide was deposited by reactive MBE deposition at $T = 435°$ C and $p_{O_2} = 10^{-6}$ mbar with a nominal thickness of 1.2 nm (it was explained in Section 3.2.1 that this coverage saturates the surface). The FePc molecular film was deposited also by MBE with coverage of 2 ML (7 Å) to obtain stronger XAS and XMCD signals.
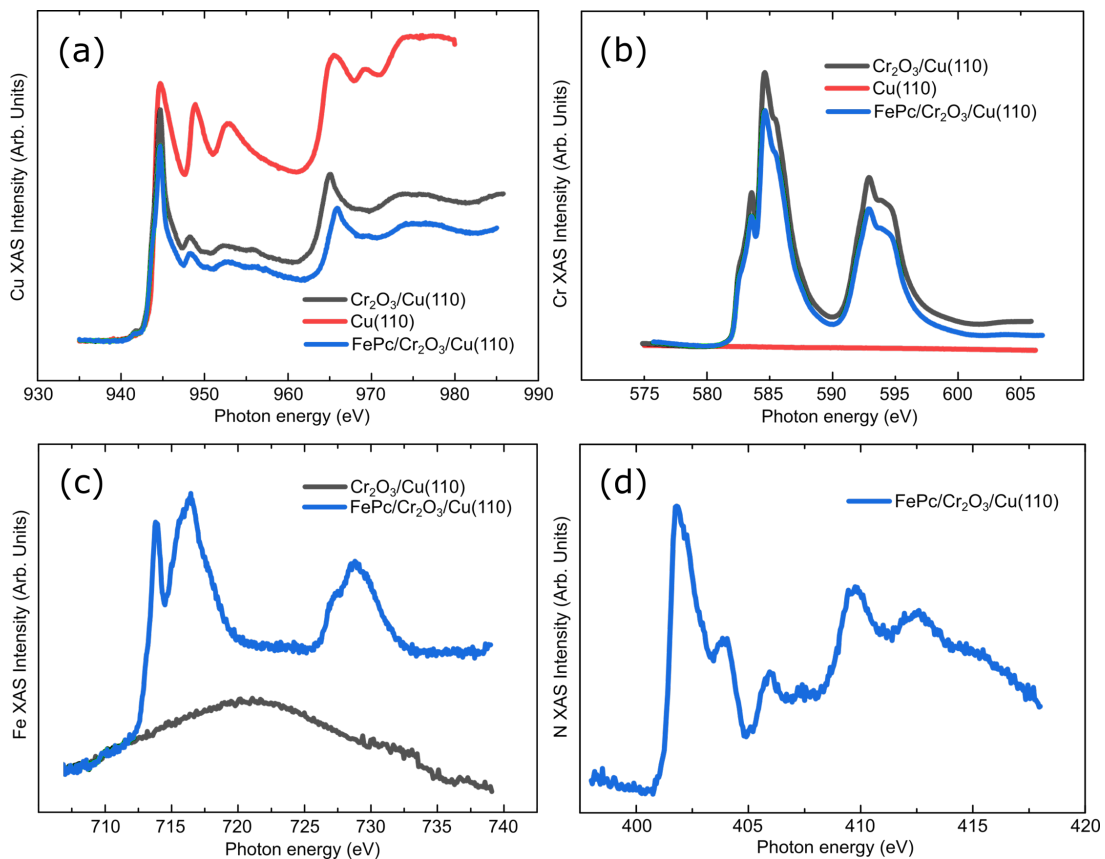


Figure 3.19: (a) XAS of Cu (L-edge); (b) Cr (L.edge); (c) Fe (L-edge); (d) N (K-edge).

X-Ray Absorption Spectroscopy (XAS) was used after each deposition to check if the materials were deposited correctly. The L-edge (corresponding to $2p_{1/2}$ and $2p_{3/2}$ core levels) XAS of Cu shown in Figure 3.19(a) is attenuated after each deposition; after the chromium deposition the L-edge XAS of Cr becomes visible (see Figure 3.19(b)) and it is attenuated after the deposition of FePc. Finally, to confirm the successful deposition of molecules, the L-edge XAS of Fe and the K-edge (corresponding to the $1s$ core level) XAS of N were measured, as shown in Figure 3.19(c) and (d).

The XMCD measurement was taken on the L-edge of Fe and it was performed at 100 K. As depicted in Figure 3.20, the circular left (CL) and circular right (CR) XAS of Fe L-edge show differences both in shape and intensity. A non-zero dichroic signal is then retrieved from the subtraction of the two absorption spectra of the central Fe atom of iron phthalocyanines, revealing that a spin-polarization has been induced in the Fe $2p$ states, and it is indicative of ferromagnetic ordering. A possible explanation for this magnetic
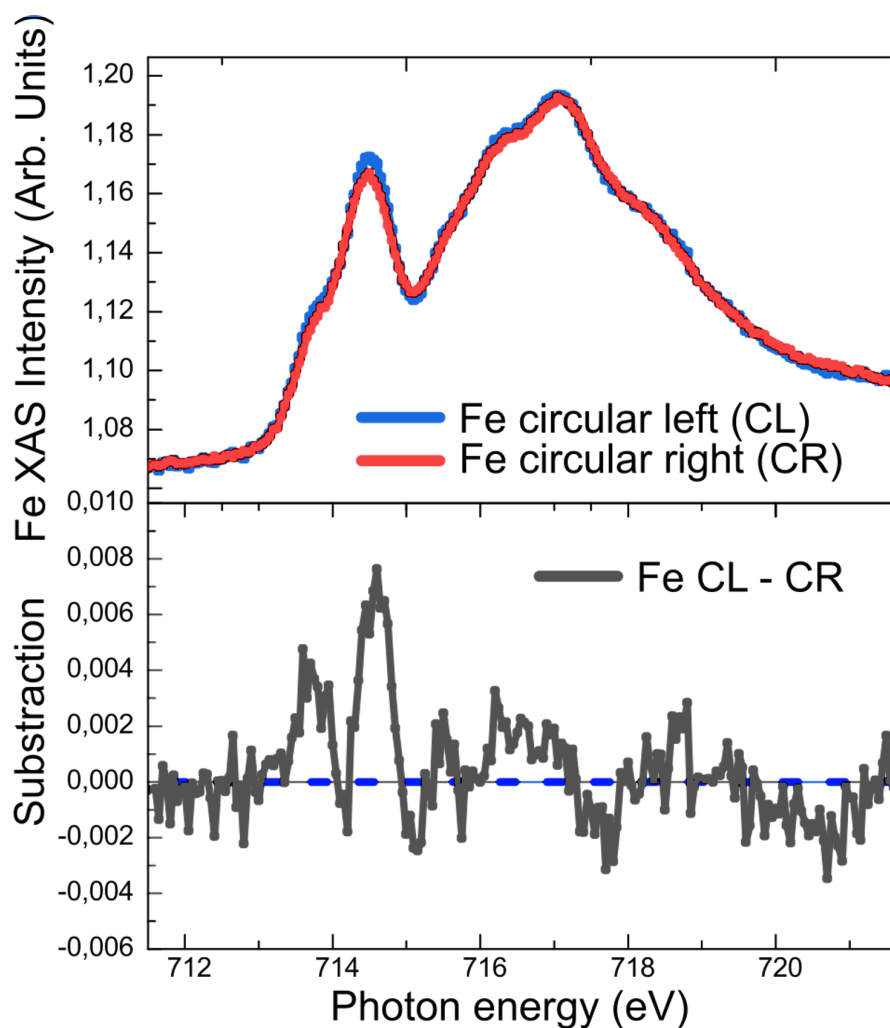


Figure 3.20: XMCD of Fe (L-edge).

polarization of $Fe^{2+}$ states can be found in the coupling of the molecular overlayer with the last layer of $Cr_2O_3$. The $Cr_2O_3(0001)$ is, in fact, a non-magnetically compensated surface. As it is visible in Figure 3.21, in each Cr layer on the (0001) plane there is an imbalance between up and down magnetic moments. Each layer is magnetically compensated by the upper one, because of the antiferromagnetic coupling. Thus, the surface layer remains uncompensated: the $Fe^{2+}$ ions of the molecular overlayer are coupled to the topmost layer of chromium oxide, and this results in the ferromagnetic ordering observed with XMCD.
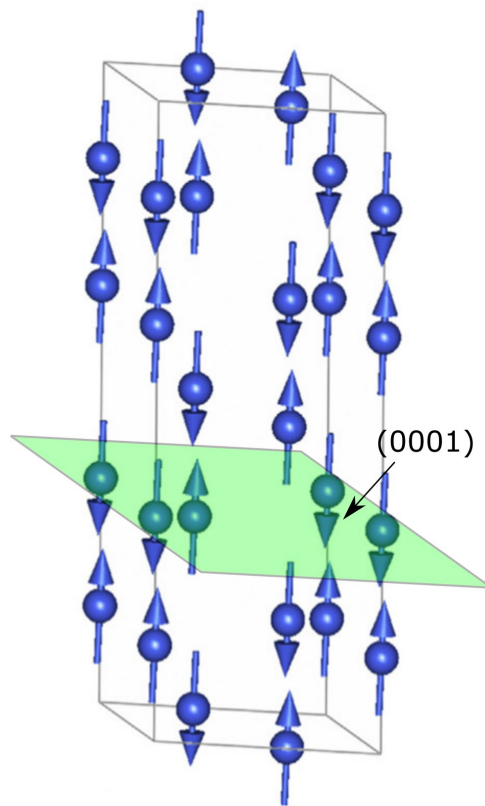


Figure 3.21: Magnetic structure of $Cr_2O_3$ along the (0001) plane. Each layer of Cr is magnetically compensated by the upper one because of the antiferromagnetic coupling.

# Conclusions

In this work, the growth of an iron phthalocyanine organic film has been performed on $Cr_2O_3/Cu(110)$. As a first step, the growth of $Cr_2O_3$ has been characterized on two copper substrates, $Cu(110)$ and $Cu(111)$. The oxide growth is non-optimal in both cases, because the Scanning Tunneling Microscopy (STM) measurements have shown that the oxide forms tall islands of 1 nm of height instead of growing layer by layer. While the islands of $Cr_2O_3/Cu(110)$ tend to remain at the same height and to become larger as the coverage increases, in the case of $Cr_2O_3/Cu(111)$ the islands become higher, up to 2-2.5 nm. For this reason, the FePc film was not grown on $Cr_2O_3/Cu(111)$, but only on $Cr_2O_3/Cu(110)$. Low Energy Electron Diffraction (LEED) has revealed that in both cases the oxide is crystalline, and in particular, the lattice estimation for $Cr_2O_3/Cu(110)$ shows that the oxide undergoes a CrO surface reconstruction. The X-Ray Absorption Spectroscopy (XAS) measurement for $Cr_2O_3/Cu(110)$ has shown that the oxide grows with the correct stoichiometry.

The FePc film was grown on $Cr_2O_3/Cu(110)$. Despite the non-optimal surface morphology of the oxide, the STM measurements have revealed that the molecules grow on top of the oxide with a planar geometry. This highlights a rather strong interaction between the FePcs and the chromium oxide layer, a fact that is not trivial because the interaction of molecules with oxides is usually weak. However, while it was possible to observe the formation of an ordered layer for coverage below a monolayer, no long-range order was observed for full monolayer coverage.

The magnetic properties of the organic layer have been investigated through X-Ray Magnetic Circular Dichroism (XMCD). The results showed that a spin-polarization is induced in the $Fe^{2+}$ $2p$ states of the molecules, indicating a ferromagnetic ordering that is likely to result from the interaction of the molecular layer with the topmost layer of chromium oxide. The $Cr_2O_3(0001)$ surface, in fact, is non-magnetically compensated and this is believed to be the origin of the molecules-oxide interaction.

# Bibliography

[1] Stefano Sanvito. Molecular spintronics. *Chem. Soc. Rev.*, 40:3336–3355, 2011.

[2] W J M Naber, S Faez, and W G van der Wiel. Organic spintronics. *Journal of Physics D: Applied Physics*, 40(12):R205–R228, jun 2007.

[3] Amin Salehi, Xiangyu Fu, Dong-Hun Shin, and Franky So. Recent advances in oled optical design. *Advanced Functional Materials*, 29(15):1808803, 2019.

[4] Michele Muccini. A bright future for organic field-effect transistors. *Nature Materials*, 5(8):605–613, 2006.

[5] C. Barraud, C. Deranlot, P. Seneor, R. Mattana, B. Dlubak, S. Fusil, K. Bouze-houane, D. Deneuve, F. Petroff, and A. Fert. Magnetoresistance in magnetic tunnel junctions grown on flexible organic substrates. *Applied Physics Letters*, 96(7):072502, 2010.

[6] Dali Sun, Eitan Ehrenfreund, and Z. Valy Vardeny. The first decade of organic spintronics research. *Chem. Commun.*, 50:1781–1793, 2014.

[7] Jagannath Devkota, Rugang Geng, Ram Chandra Subedi, and Tho Duc Nguyen. Organic spin valves: A review. *Advanced Functional Materials*, 26(22):3881–3898, 2016.

[8] Marco Gobbi, Emanuele Orgiu, and Paolo Samorì. When 2d materials meet molecules: Opportunities and challenges of hybrid organic/inorganic van der Waals heterostructures. *Advanced Materials*, 30(18):1706103, 2018.

[9] Sophie Delprat, Marta Galbiati, Sergio Tatay, Benoît Quinard, Clément Barraud, Frédéric Petroff, Pierre Seneor, and Richard Mattana. Molecular spintronics: the role of spin-dependent hybridization. *Journal of Physics D: Applied Physics*, 51(47):473001, sep 2018.

[10] Stefano Sanvito. The rise of spinterface science. *Nature Physics*, 6(8):562–564, 2010.

[11] F. Djeghloul, G. Garreau, M. Gruber, L. Joly, S. Boukari, J. Arabski, H. Bulou,

F. Scheurer, A. Hallal, F. Bertran, P. Le Fèvre, A. Taleb-Ibrahimi, W. Wulfhekel, E. Beaurepaire, S. Hajjar-Garreau, P. Wetzel, M. Bowen, and W. Weber. Highly spin-polarized carbon-based spinterfaces. *Carbon*, 87:269–274, 2015.

[12] Rui Pang, Xingqiang Shi, and Michel A. Van Hove. Manipulating magnetism at organic/ferromagnetic interfaces by molecule-induced surface reconstruction. *Journal of the American Chemical Society*, 138(12):4029–4035, 2016. PMID: 26966934.

[13] Fatma Al Ma'Mari, Timothy Moorsom, Gilberto Teobaldi, William Deacon, Thomas Prokscha, Hubertus Luetkens, Steve Lee, George E. Sterbinsky, Dario A. Arena, Donald A. MacLaren, Machiel Flokstra, Mannan Ali, May C. Wheeler, Gavin Burnell, Bryan J. Hickey, and Oscar Cespedes. Beating the stoner criterion using molecular interfaces. *Nature*, 524(7563):69–73, 2015.

[14] F. Djeghloul, F. Ibrahim, M. Cantoni, M. Bowen, L. Joly, S. Boukari, P. Ohresser, F. Bertran, P. Le Fèvre, P. Thakur, F. Scheurer, T. Miyamachi, R. Mattana, P. Seneor, A. Jaafar, C. Rinaldi, S. Javaid, J. Arabski, J. P Kappler, W. Wulfhekel, N. B. Brookes, R. Bertacco, A. Taleb-Ibrahimi, M. Alouani, E. Beaurepaire, and W. Weber. Direct observation of a highly spin-polarized organic spinterface at room temperature. *Scientific Reports*, 3(1):1272, 2013.

[15] Mirko Cinchetti, V. Alek Dediu, and Luis E. Hueso. Activating the molecular spinterface. *Nature Materials*, 16(5):507–515, 2017.

[16] O. Gomonay, T. Jungwirth, and J. Sinova. Concepts of antiferromagnetic spintronics. *physica status solidi (RRL) – Rapid Research Letters*, 11(4):1700022, 2017.

[17] J. Železný, P. Wadley, K. Olejník, A. Hoffmann, and H. Ohno. Spin transport and spin torque in antiferromagnetic devices. *Nature Physics*, 14(3):220–228, 2018.

[18] Matthias B. Jungfleisch, Wei Zhang, and Axel Hoffmann. Perspectives of antiferromagnetic spintronics. *Physics Letters A*, 382(13):865–871, 2018.

[19] O. Gomonay, V. Baltz, A. Brataas, and Y. Tserkovnyak. Antiferromagnetic spin textures and dynamics. *Nature Physics*, 14(3):213–216, 2018.

[20] Arne Brataas, Hans Skarsvåg, Erlend G. Tveten, and Eirik Løhaugen Fjærbu. Heat transport between antiferromagnetic insulators and normal metals. *Phys. Rev. B*, 92:180414, Nov 2015.

[21] Tobias Kampfrath, Alexander Sell, Gregor Klatt, Alexej Pashkin, Sebastian Mährlein, Thomas Dekorsy, Martin Wolf, Manfred Fiebig, Alfred Leitenstorfer, and

Rupert Huber. Coherent terahertz control of antiferromagnetic spin waves. *Nature Photonics*, 5(1):31–34, 2011.

[22] Xiao-Xiao Zhang, Lizhong Li, Daniel Weber, Joshua Goldberger, Kin Fai Mak, and Jie Shan. Gate-tunable spin waves in antiferromagnetic atomic bilayers. *Nature Materials*, 19(8):838–842, 2020.

[23] Alexei Bagrets, Stefan Schmaus, Ali Jaafar, Detlef Kramczynski, Toyo Kazu Yamada, Mébarek Alouani, Wulf Wulfhekel, and Ferdinand Evers. Single molecule magnetoresistance with combined antiferromagnetic and ferromagnetic electrodes. *Nano Letters*, 12(10):5131–5136, 2012. PMID: 22989203.

[24] X. Sun, B. Wang, A. Pratt, and Y. Yamauchi. Magnetic moment enhancement and spin polarization switch of the manganese phthalocyanine molecule on an irmn(100) surface. *The Journal of Chemical Physics*, 141(3):034703, 2014.

[25] Yangfan Shao, Rui Pang, Hui Pan, and Xingqiang Shi. Fullerene antiferromagnetic reconstructed spinterface subsurface layer dominates multi-orbitals spin-splitting and large magnetic moment in c60, 2016.

[26] R.D. Gould. Structure and electrical conduction properties of phthalocyanine thin films. *Coordination Chemistry Reviews*, 156:237–274, 1996.

[27] H. Laurs and G. Heiland. Electrical and optical properties of phthalocyanine films. *Thin Solid Films*, 149(2):129–142, 1987.

[28] B. W. Dale, R. J. P. Williams, C. E. Johnson, and T. L. Thorp. S = 1 spin state of divalent Iron. Magnetic properties of phthalocyanine Iron (II). *The Journal of Chemical Physics*, 49(8):3441–3444, 1968.

[29] M. Evangelisti, J. Bartolomé, L. J. de Jongh, and G. Filoti. Magnetic properties of $\alpha$-Iron(II) phthalocyanine. *Phys. Rev. B*, 66:144410, Oct 2002.

[30] Christian G. Claessens, Uwe Hahn, and Tomás Torres. Phthalocyanines: From outstanding electronic properties to emerging applications. *The Chemical Record*, 8(2):75–97, 2008.

[31] H. S. Soliman, M. M. El Nahass, A. M. Farid, A. A. M. Farag, and A. A. El Shazly. Structural and transport properties of evaporated iron phthalocyanine (FePc) thin films. *The European Physical Journal - Applied Physics*, 21(3):187–193, 2003.

[32] Christian G. Claessens, Werner J. Blau, Michael Cook, Michael Hanack, Roeland J. M. Nolte, Tomás Torres, and Dieter Wöhrle. Phthalocyanines and phthalocyanine

analogues: The quest for applicable optical properties. *Monatshefte für Chemie / Chemical Monthly*, 132(1):3–11, 2001.

[33] B. Tunhoo and J. Nukeaw. Structural and optical properties of low temperature evaporated iron phthalocyanine thin films. *Materials Research Innovations*, 13(3):145–148, 2009.

[34] Hari Singh Nalwa and Atsushi Kakuta. Third-order non-linear optical properties of donor- and acceptor-substituted metallophthalocyanines. *Thin Solid Films*, 254(1):218–223, 1995.

[35] Aivar Tarre, Jaan Aarik, Hugo Mändar, Ahti Niilisk, Rainer Pärna, Raul Rammula, Teet Uustare, Arnold Rosental, and Väino Sammelselg. Atomic layer deposition of cr2o3 thin films: Effect of crystallization on growth and properties. *Applied Surface Science*, 254(16):5149–5156, 2008.

[36] M. Catti, G. Sandrone, G. Valerio, and R. Dovesi. Electronic, magnetic and crystal structure of cr2o3 by theoretical methods. *Journal of Physics and Chemistry of Solids*, 57(11):1735–1741, 1996.

[37] Øyvind Borck and Elsebeth Schröder. Adsorption of methanol and methoxy on the $\alpha$-Cr$_2$O$_3$(0001) surface. *Journal of Physics: Condensed Matter*, 18(48):10751–10763, nov 2006.

[38] N.O. Golosova, D.P. Kozlenko, S.E. Kichanov, E.V. Lukin, H.-P. Liermann, K.V. Glazyrin, and B.N. Savenko. Structural and magnetic properties of cr2o3 at high pressure. *Journal of Alloys and Compounds*, 722:593–598, 2017.

[39] Hans Lüth. *Solid Surfaces, Interfaces and Thin Films*. Springer, Cham, Fifth edition, 2010.

[40] Gerrit van der Laan and Adriana I. Figueroa. X-ray magnetic circular dichroism—A versatile tool to study magnetism. *Coordination Chemistry Reviews*, 277-278:95–129, 2014. Following Chemical Structures using Synchrotron Radiation.

[41] M. Asa, G. Vinai, J. L. Hart, C. Autieri, C. Rinaldi, P. Torelli, G. Panaccione, M. L. Taheri, S. Picozzi, and M. Cantoni. Interdiffusion-driven synthesis of tetragonal chromium (iii) oxide on BaTio$_3$. *Phys. Rev. Materials*, 2:033401, Mar 2018.

[42] P. Palmgren, T. Angot, C. I. Nlebedim, J.-M. Layet, G. Le Lay, and M. Göthelid. Ordered phthalocyanine superstructures on Ag(110). *The Journal of Chemical Physics*, 128(6):064702, 2008.

[43] Lorenzo Massimi, Marco Angelucci, Pierluigi Gargiani, Maria Grazia Betti, Silvia Montoro, and Carlo Mariani. Metal-phthalocyanine ordered layers on Au(110): Metal-dependent adsorption energy. *The Journal of Chemical Physics*, 140(24):244704, 2014.

[44] Fang Hu, Hongying Mao, Hanjie Zhang, Ke Wu, Yiliang Cai, and Pimo He. Electronic and structural properties at the interface between iron-phthalocyanine and Cu(110). *The Journal of Chemical Physics*, 140(9):094704, 2014.

# List of Figures

# Acknowledgements

I would like to thank my supervisor Andrea and my co-supervisor Alberto for the opportunity they gave me with this research experience, and also for the support they gave me with the writing of this thesis. I would also like to thank Michele and Alessio for following me every day in the laboratory during these last months.

A special thank goes to all my friends at Engineering Physics, for the support they gave me through this journey, but most of all for all the lunchbreaks that we spent playing cards.

Finally, the biggest thank of all goes to my family, for always believing in me and always supporting me in whatever decision I make.